Inter-hemispheric asymmetry in the sea-ice response to volcanic forcing simulated by MPI-ESM (COSMOS-Mill)

Zanchettin Davide[1*], Oliver Bothe[2], Claudia Timmreck[1], Jürgen Bader[1], Alexander Beitsch[1], Hans-F. Graf[3], Dirk Notz[1], and Johann H. Jungclaus[1]

[1] Max Planck Institute for Meteorology, Bundesstr. 53, 20146 Hamburg, Germany

[2] Leibniz Institute of Atmospheric Physics at the University of Rostock, Kühlungsborn, Germany

[3] University of Cambridge, Centre for Atmospheric Science, Downing Place, Cambridge CB2 3EN, United Kingdom

* corresponding author: davide.zanchettin@mpimet.mpg.de

Abstract

The decadal evolution of Arctic and Antarctic sea ice following strong volcanic eruptions is investigated in four climate simulation ensembles performed with the COSMOS-Mill version of the Max Planck Institute-Earth System Model. The ensembles differ in the magnitude of the imposed volcanic perturbations, with sizes representative of historical tropical eruptions (1991 Pinatubo and 1815 Tambora) and of tropical and extra-tropical "supervolcano" eruptions. A post-eruption Arctic sea-ice expansion is robustly detected in all ensembles, while Antarctic sea ice responds only to "supervolcano" eruptions, undergoing an initial short-lived expansion and a subsequent prolonged contraction phase. Strong volcanic forcing therefore emerges as a potential source of inter-hemispheric interannual-to-decadal climate variability, although the inter-hemispheric signature is weak in the case of historical-size eruptions. The post-eruption inter-hemispheric decadal asymmetry in sea ice is interpreted as a consequence mainly of different exposure of Arctic and Antarctic regional climates to induced meridional heat transport changes and of dominating local feedbacks that set in within the Antarctic region. "Supervolcano" experiments help clarifying differences in simulated hemispheric internal dynamics related to imposed negative net radiative imbalances, including the relative importance of the thermal and dynamical components of the sea-ice response. "Supervolcano" experiments could therefore serve the assessment of climate models' behavior under strong external forcing conditions and, consequently, favor advancements in our understanding of simulated sea-ice dynamics.

1. Introduction

Polar regional climates are in the focus of Earth system investigations owing to their strong sensitivity to external forcing and associated implications for the global climate. The so-called “polar amplification” of climate signals is mainly a consequence of positive feedbacks involving snow cover and sea ice, and it emerges more robustly in the Northern than in the Southern Hemisphere [e.g., *Parkinson*, 2004]. The different behavior of Arctic and Antarctic sea ice is largely explained by the different geographical characteristics of the two polar regions: The semi-enclosed Arctic Ocean limits sea-ice mobility and favors sea-ice thickening and persistence while making Arctic sea ice strongly susceptible to changes in the Atlantic Ocean’s northward heat transport and to anomalous atmospheric heat inflows from the surrounding landmasses. Antarctic sea-ice, by contrast, forms around the Antarctica landmass in the open Southern Ocean, its northern boundary being set by the circumpolar system of southern mid-latitude westerly winds and ocean currents. This system makes Antarctic sea ice strongly subject to equatorward drifting and melting - which explains its weak persistence - while limiting its exposure to global changes and associated anomalous atmospheric and oceanic meridional heat flows [e.g., *Zhang*, 2007, 2013]. Still, important processes driving this critical component of the Earth system remain unresolved and, hence, not robustly simulated by coupled global circulation models and Earth system models [e.g., *Maksym et al.*, 2012; *Turner et al.*, 2013; Knight, 2014]. Aiming at a better understanding of simulated global sea-ice behavior and of its sensitivity to external forcing, this study investigates the decadal evolution of Arctic and Antarctic sea ice in a set of idealized volcanically-forced experiments conducted with a full-complexity Earth system model. Focus is on inter-hemispheric differences in the sea-ice response.

Observations covering the past three decades point to an inter-hemispheric asymmetry in recent sea-ice cover evolution: While the decline in Arctic total sea-ice cover is among the most notable features related to present climate change [e.g., *Notz and Marotzke*, 2012; *Stroeve et al.*, 2012; *Wang and Overland*, 2012], the Antarctic total sea-ice cover has remained steady, or even increased slightly [*Stammerjohn et al.*, 2012; *Massonnet et al.*, 2013]. The Antarctic sea-ice increase has been largest in autumn, with a dipole of a regionally significant positive trend in the Ross Sea and a negative trend in the Amundsen-Bellingshausen Sea [*Turner et al.*, 2009]. Despite generally improved representations of observed sea-ice climatology and evolution [*Stroeve et al.*, 2012], state-of-the-art coupled climate models fail to reproduce the observed increase in Antarctic total sea-ice cover over the last 30 years, indicating that the underlying processes are not yet simulated correctly [*Turner et al.*, 2013]. Therefore, understanding the behavior of Antarctic sea ice and improving its representation in climate models has high priority for the aim of correctly reproducing the observed Arctic/Antarctic sea-ice dichotomy [*King*, 2014].

Internal climate variability in historical climate simulations contributes substantially to both Arctic and Antarctic sea-ice variability [*Stroeve et al.*, 2012; *Polvani and Smith*, 2013]. As a consequence, simulated trends in Arctic sea ice over the last ~ 30 years are generally smaller than suggested by satellite-derived sea-ice products [*Stroeve et al.*, 2012], while simulated trends in Antarctic sea ice are characterized by large inter-model differences [*Polvani and Smith*, 2013]. Therefore, no conclusive assessment is available about whether the observed sea-ice asymmetry reflects a characteristic (either internally-generated or externally-forced) inter-hemispheric mode of polar climate variability or, alternatively, an extraordinary externally-forced feature.

Hinting towards the first hypothesis, a multicentennial control climate simulation features interdecadal periods characterized by positive trends in Antarctic sea-ice cover comparable to that observed during the last ~ 30 years [*Turner et al.*, 2009]. The 20th century experienced several decades of inter-hemispheric contrast in the temperature trend [e.g., *Brohan et al.*, 2006; *Duncan et al.*, 2010; *Chylek et al.*, 2010]. Inter-hemispheric out-of-phase multidecadal temperature fluctuations also emerge from reconstructed regional and continental-scale temperature variability during the last millennium and beyond [*Duncan et al.*, 2010; *Ahmed et al.*, 2013]. Paleoclimatic records for the last glacial maximum similarly indicate that heterogeneity and non-synchronic behavior of polar ice sheets and glacier behavior is a characteristic feature of millennial-scale climate variability [*Schaefer et al.*, 2009; *Weber et al.*, 2011; *Shakun et al.*, 2012]. The core processes implicated in these low-frequency inter-hemispheric climate fluctuations may be similarly important for sub-centennial Arctic/Antarctic climate variability.

The hypothesis of an externally-forced inter-hemispheric asynchronism implies the existence of regional forcing agents and/or of response mechanisms to global forcing agents that are capable to drive a (multi)decadal inter-hemispheric climate offset. Stratospheric ozone depletion in the Southern Hemisphere is among the regional factors capable of affecting Antarctic sea ice, especially so through tendential changes induced in the large-scale tropospheric circulation of the Southern Hemisphere [*Gillett and Thompson*, 2003; *Turner et al.*, 2009]. Coupled climate simulations including time-varying stratospheric ozone, however, do not support a causal relationship between stratospheric ozone depletion and increased Antarctic sea ice [*Sigmond and Fyfe*, 2014].

Strong volcanic eruptions are a likely candidate for a natural forcing agent that acts globally and yet causes pronounced differences in the inter-hemispheric response: For the Arctic, climate simulations indicate explosive volcanism as a major source of near-decadal [*Stenchikov et al.*, 2009; *Segschneider et al.*, 2012; *Zanchettin et al.*, 2012, 2013a] and multidecadal-to-centennial [*Zhong et al.*, 2011] fluctuations in the total sea-ice area. A volcanically-forced Arctic sea-ice expansion has been suggested to be pivotal for the onset and sustenance of the Little Ice Age [*Miller et al.*, 2012; *Schleussner and Feulner*, 2012], the prolonged widespread cold period spanning the 15^{th}-18^{th} centuries. The same period features, however, a pronounced reduction of late-summer Arctic total sea-ice extent in a recent millennial reconstruction [*Kinnard et al.*, 2011], a counterintuitive behavior that highlights the complexity of the dynamical processes behind low-frequency variability of sea ice and our still limited knowledge about the climate state and the mechanism(s) behind specific anomalous episodes [e.g., *Zanchettin et al.*, 2013a].

The scientific literature lacks studies about the susceptibility of Antarctic sea ice to volcanic forcing. There are no sufficiently-resolved reconstructions of Antarctic sea ice to assess anomalies during periods of strong volcanism before the satellite era, or they lack context as, for instance, the so-far punctual estimate of Antarctic sea-ice extent of September 1964 [*Meier et al.*, 2013] during the aftermath of the 1963 eruption of Mount Agung. Diagnosed dynamical atmospheric responses to the strongest 20^{th} century eruptions are not robust in the Southern Hemisphere in observations and especially in simulations [e.g., *Robock et al.*, 2007; *Karpechko et al.*, 2010; *Charlton-Perez et al.*, 2013]. Generalizing assessments based on the 20th century eruptions is prevented by the paucity and limited magnitude of the considered events, and by their concomitance with known potential disturbances to the post-eruption Antarctic climate evolution. Such disturbances include internal (e.g., a large warm event of the El Niño—Southern Oscillation or ENSO) and external ones. The latter would include, e.g., a period of weak solar activity [*Barlyaeva et al.*, 2009] and the ozone hole [*Bitz and Polvani*, 2012]. In fact, Antarctic sea ice expands considerably in the aftermath of a "supervolcano" eruption simulated by a coupled climate model [*Jones et al.*, 2005]. Confronting the "supervolcano" response with the lack of a clear response to 20th century eruptions poses the question of whether a possible southern-hemispheric dynamical response remains elusive due to a low signal-to-noise ratio for historical-size eruptions.

In this study, we assess the simulated inter-hemispheric sea-ice response to idealized volcanic perturbations by pursuing the following strategy: (i) investigating ensembles of Earth-system-model simulations that are sufficiently populated to yield a robust estimate of the expected forced response; (ii) comparing ensemble-average simulated responses induced by volcanic perturbations of different magnitude, ranging from that of a 1991 Pinatubo-size eruption to those of "supervolcano"-size eruptions. By including the latter we explore responses to forcing amplitudes pushing the simulated climate to its extremes. In the past, comprehensive assessments of climate responses under idealized external forcings as those used here have been proven valuable to understand simulated climate features and mechanisms and, consequently, to delimit the validity of model-based inferences about climate dynamics and variability, as well as to compare the performance of different climate models [e.g., *Stouffer et al.*, 2006]. Accordingly, we focus on the inter-hemispheric asymmetry in simulated sea-ice behavior, but we also discuss possible limitations in the realism of the simulated sea-ice behavior in the light of the ocean/atmosphere/sea-ice coupled dynamics inferred from the analysis of the simulation ensemble. Our assessment therefore delineates how deficiencies in, e.g., the representation of the Southern Ocean [e.g., *Russell et al.*, 2006; *Weijer et al.*, 2012; *Heuzé et al.*, 2013; *Salleé et al.*, 2013], of Southern Hemisphere's atmospheric circulation

[*Simpson et al.*, 2012; *Stössel et al.*, 2011] and of sea-ice processes relevant for the Antarctic [*Landrum et al.*, 2012; *Maksym et al.*, 2012] may reverberate on simulated transient global climate variability.

We proceed as follows. First, in Section 2 we detail the experimental design of this study, including the Earth system model, the simulations and the diagnostic tools. In Section 3 we present the characteristics of the simulated climate responses to the imposed forcing, focusing on post-eruption fluctuations in Arctic and Antarctic sea ice and highlighting inter-hemispheric differences in the (forced) post-eruption signals and associated dynamics. We discuss our results in Section 4 and provide conclusive remarks in Section 5.

2. Data and methods

We use the Max Planck Institute-Earth system model (MPI-ESM) in its COSMOS-Mill version. The name of this version reflects the fact that the Community Earth System Modeling (COSMOS) community used it for its Millennium Experiment, as described by *Jungclaus et al.* [2010.], who provide a detailed description of the model setup. MPI-ESM-COSMOS-Mill is based on the atmospheric general circulation model ECHAM5 [*Roeckner et al.*, 2006] coupled with the ocean model MPIOM [*Marsland et al.*, 2003; *Jungclaus et al.*, 2006] via the OASIS3 coupler. Modules for terrestrial biosphere (JSBACH, see: *Raddatz et al.*, 2007) and for ocean biogeochemistry (HAMOCC, see: *Wetzel et al.*, 2005) allow for an interactive representation of the carbon cycle. The ECHAM5/MPIOM coupled general circulation model participated to the Coupled Model Intercomparison Project 3 (CMIP3), and has been extensively evaluated in that context. *Jungclaus et al.* (2006) describe the general climatological oceanic features of the ECHAM5/MPIOM included Arctic and Antarctic sea ice: simulated sea-ice concentrations generally compare well to the observations in both hemispheres; seasonal variation and mean distribution of Antarctic sea-ice concentrations are overall satisfactorily simulated, though the model tends to underestimate winter sea-ice concentration in the Weddell Sea and the Ross Sea. *Koldunov et al.* (2010) provide a detailed evaluation of Arctic sea-ice variability simulated by ECHAM5/MPIOM compared against late 20th century observations. *Notz and Marotzke* [2012] showed that the internal variability of Arctic sea-ice coverage as simulated by ECHAM5/MPIOM agrees favorably with the observed internal variability.

In MPI-ESM-COSMOS-Mill, ECHAM5 is run in its T31L19 configuration, corresponding to a spatial resolution of 3.75° x 3.75° and 19 vertical levels with the highest one (i.e., the model top) set at 10 hPa. The model's low top restrict the description of stratospheric and coupled stratosphere-troposphere dynamics [e.g., *Omrani et al.*, 2013], which may affect the dynamical atmospheric response to volcanic forcing [e.g., *Charlton-Perez et al.*, 2013]. MPIOM is run in its standard configuration GR30L40, corresponding to a horizontal grid-spacing of about 3.0° and 40 vertical levels. It embeds a dynamic-thermodynamic Hibler-type sea-ice model. A detailed description of the treatment of sub grid-scale mixing and of the sea-ice dynamics and thermodynamics implemented in MPIOM is provided by *Marsland et al.* [2003].

A number of studies have evaluated the climate and its variability as simulated by MPI-ESM-COSMOS-Mill against observations, proxy-based reconstructions and within a multi-model framework [e.g., *Henriksson et al.*, 2012; *Beitsch et al.*, 2013; *Bothe et al.*, 2013; *Fernández-Donado et al.*, 2013; *Schubert et al.*, 2013; *Zanchettin et al.*, 2012, 2013a,b]. In particular, *Beitsch et al.* [2013] showed that MPI-ESM-COSMOS-Mill spontaneously generates positive decadal-scale temperature anomalies in the Arctic region that are compatible with the observed episode known as the "early twentieth century warming". *Tietsche et al*. [2011] explored recovery mechanisms of Arctic summer sea ice through perturbation experiments conducted with ECHAM5/MPIOM in the same configuration as MPI-ESM-COSMOS-Mill. *Li et al.* [2013] used idealized global warming simulations performed with ECHAM5/MPIOM in the same configuration to explore the long-term stability of Arctic and Antarctic sea ice against slow changes in atmospheric CO_2 concentration. Climatological characteristics of sea-ice concentration simulated by MPI-ESM-COSMOS-Mill are provided in the supplement (Figures S1 and S2). They agree well with those described by *Jungclaus et al.* [2006] for ECHAM5/MPIOM.

Four simulation ensembles are considered describing the climatic effects of idealized volcanic perturbations of different magnitude, up to "supervolcano"-size eruptions. The four ensembles consist of (i) ten simulations forced by a 1991 Pinatubo-like tropical eruption, (ii) ten simulations forced by a 1815 Tambora-like tropical eruption, (iii) five simulations forced by a Young Toba Tuff (Toba)-like eruption, i.e., a tropical eruption with 100-times the emission strength of the Pinatubo eruption, and (iv) ten simulations forced by a Yellowstone-like eruption (i.e., same as Toba, but located in the Northern Hemisphere's mid-latitudes). In the following, we refer to the ensembles avoiding the volcanoes' specific names to highlight their idealized character. We thereafter refer to the Pinatubo and Tambora simulations/eruptions as "historical" (namely HIST1 and HIST2, respectively), since these eruptions are representative of the magnitude of volcanic eruptions that occurred during the last millennium. The Toba and Yellowstone "supervolcano" ensembles are referred to as SUPER1 and SUPER2, respectively. HIST2 corresponds to the VO2 ensemble in *Zanchettin et al.* [2013a]. SUPER1 entails the simulations used in *Timmreck et al.* [2010, 2012]. SUPER2 simulations are those described in *Segschneider et al.* [2012]. Each ensemble consists of simulations differing only in their initial climate states, which are sampled from a multi-millennial pre-industrial control simulation [as used in *Timmreck et al.*, 2010, and *Zanchettin et al.*, 2013a]. In HIST1, SUPER1 and SUPER2 the eruptions start in June of the first integration year. In HIST2 the eruption starts in April, according to historical reconstructions of the 1815 Tambora event (*Crowley et al.* [2008], *Crowley and Untermann* [2012]). HIST2 simulations include the eruptions reconstructed for the subsequent decades, e.g., the Cosiguina eruption in the early 1830s [*Zanchettin et al.*, 2013a].

Volcanic forcing implemented in MPI-ESM is based on zonally-averaged time series of aerosol optical depth (AOD) at 0.55 μm and of effective particle radius (R_{eff}). For HIST2, we use the reconstructed 10-day average values of AOD and R_{eff} by *Crowley et al.* [2008]. Data are provided for four equal-area latitudinal bands (90ºS-30ºS, 30ºS-0º, 0º-30ºN and 30ºN-90ºN). Volcanic aerosols are vertically distributed between 30 and 70 hPa, with a maximum at 50 hPa [*Timmreck et al.,* 2009]. For the other ensembles, AOD and R_{eff} are estimated following the two-step approach described by *Timmreck et al.* [2010]. Briefly summarizing it: in the first step the formation of volcanic sulfate aerosols is calculated from an initial volcanic sulfur injection in the stratosphere by the middle atmosphere version of the aerosol climate model ECHAM/HAM [*Stier et al.,* 2005;

Niemeier et al., 2009]; in the second step, the zonally-averaged monthly time series of the so calculated AOD and R_{eff} values are used as external forcing in MPI-ESM. Due to subsequent temporal interpolation of input data by ECHAM5, in MPI-ESM the eruption is tailed in the month preceding its occurrence in ECHAM/HAM.

In all simulations, the time-dependent AOD and R_{eff} values are used to calculate online the optical parameters of the ECHAM5 radiation scheme, including extinction, single-scattering albedo and asymmetry factor for the six solar bands (0.185-4 μm), and extinction for the 16 long-wave wavelength bands (3.3-100 μm). Aerosol sizes are assumed to be distributed with a constant standard deviation of 1.8 μm.

The global-average air surface temperature drop after the 1991 Pinatubo eruption in sensitivity experiments conducted with MPI-ESM is comparable with observations [*Timmreck et al.*, 2009]. Global and hemispheric near-surface air temperature changes in a full-forcing COSMOS-Mill simulation ensemble around the Tambora eruption employing the same volcanic forcing input as the HIST2 ensemble are compatible with estimates from observations and reconstructions [*Zanchettin et al.*, 2013a].

Responses are diagnosed through analysis of ensemble-averages. For time series, we use deseasonalized and then low-pass filtered values. Seasonality is computed based on control-run data and then subtracted from all data. Filtering consists of 3-month centered running-mean for atmospheric variables, and 13-month centered running-mean for oceanic and sea-ice variables, unless specified otherwise. Anomalies are evaluated as deviations from the pre-eruption climatology, defined as the mean climate state during the ten years/winters/summers preceding the eruption. Post-eruption years are progressively numbered starting from the year of the eruption, which is defined as year 0.

A Monte-Carlo approach is used to estimate the statistical significance of the forced signals [e.g., *Graf and Zanchettin*, 2012]. Specifically, the ensemble-average signals obtained from an ensemble of n forced simulations are compared with a large set of analog ensemble-average signals (here 500) obtained by randomly sampling n years along the whole length of the control run. The empirical distribution yielded by these analog ensemble-average signals describes probabilistically the range explicable by internal variability alone, which we also interpret as the confidence level of corresponding signals in the forced ensembles having occurred by chance. We consider as reference the 98% range (i.e., 1st-99th percentile band) of such distribution in order to have a conservative estimate of internal variability signals. Since the procedure is only based on the random selection of years, the autocorrelation is preserved in the estimation of the significance.

Total sea-ice area in the Arctic and in the Antarctic is calculated as the areal sum of sea ice covering the ocean in the Northern and Southern Hemispheres, respectively. Analogously, total sea-ice volume is defined as the sum of local (i.e., grid-point) products of grid-cell area and grid-cell-average sea-ice thickness. The sea-ice edge is defined as the line denoting the sea-ice extent margin, i.e., the area enclosing sea-ice concentrations exceeding the 0.15 threshold (in the range [0:1], where 0 indicates no sea ice in the grid-cell and 1 indicates sea ice fully covering the grid-cell).

Meridional ocean heat transports HT are calculated at 60°N and 60°S as in *Zanchettin et al.* [2012] based on the equation: $HT = \Sigma_z \Sigma_x\, v\, T\, c_p\, \rho\, dx\, dz$, where v is the meridional velocity component, T is temperature, c_p is specific heat capacity at constant pressure, ρ is density, and dz and dx represent, respectively, the integrals along depths and longitudes. The zonal mean component of the total meridional ocean heat transports is considered to be associated with the overturning transport; the residual component is considered to describe the gyre contribution to the total meridional ocean heat transport. Accordingly, deviations of v and T from the respective zonal mean values are used in the above mentioned equation for the calculation of the gyre contribution to HT.

The meridional atmospheric energy transport around 60°N and 60°S are defined, following *Keith* [1995], as the zonal integral at, respectively, 61.23°N and 61.23°S of the convergence of the atmospheric energy transport vector $\mathbf{F}_A$, which can be written for latitude λ as:

$$F_\lambda = \int_\lambda -\nabla * \mathbf{F}_A dx = \int_\lambda -\nabla * \frac{1}{g} \int_0^{p_s} (c_p T + \Phi + Lq + k)\mathbf{v}\, dp\, dx \qquad (1)$$

where dp and dx represent, respectively, the integral along pressure levels and longitudes, $c_pT + \Phi$ represents the dry static energy, with the specific heat of the atmosphere at constant pressure c_p, temperature T, and geopotential Φ. The moist static energy is depicted by $c_pT + \Phi + Lq$, with latent heat of evaporation/condensation L, and specific humidity q. The horizontal wind vector is represented by $\mathbf{v}$. As kinetic energy k is typically a small component of the energy budget, it is ignored in the following. The small latitudinal difference between atmospheric and oceanic heat transport calculations is of negligible concern, since we do not aim to close the energy budget for the two regions.

3. Results

3.1 Imposed forcing and global/hemispheric responses

The imposed forcing is very well constrained within each of the four ensembles (Figure 1). Estimates based on top-of-atmosphere radiative anomalies for individual ensembles are consistent with previously reported ones [*Timmreck et al.*, 2010; *Segschneider et al.*, 2012; *Zanchettin et al.*, 2013a]; we therefore describe only major features and inter-ensemble differences. Especially during the first three post-eruption years, ensemble standard errors are barely distinguishable from the corresponding ensemble-average values. Peak negative anomalies in the global top-of-atmosphere net radiative flux range between ~ -3 Wm^{-2} for HIST1 and ~ -27 Wm^{-2} for SUPER2 (Figure 1c). SUPER2 leads to a slightly stronger forcing than SUPER1 in the net radiative flux estimate (Figure 1c). This highlights the dependence of the net forcing on the shape of post-eruption evolutions of the shortwave and longwave radiation flux anomalies, since these have otherwise similar peak values in the two ensembles (Figure 1a,b). The evolution of radiative fluxes is directly linked to the evolution of the volcanic aerosol mass, which builds up slower during the first post-eruption months in SUPER2 compared to SUPER1 (not shown). This seems to be the key to understanding the differences between the two “supervolcano” ensembles and the distinguishing traits of the former. The positive net flux anomaly around lags of 42 to 78 months is mainly a consequence of the ocean releasing less latent heat to the atmosphere [*Timmreck et al*., 2010; *Zanchettin et al*., 2013a].

On the global scale, the four ensembles depict significant post-eruption drops in surface (2 meters) air temperature and precipitation (Figure 2a,b). Cold temperature anomalies consistently peak in the boreal summer-autumn of year 1, i.e. slightly after the peak in the forcing (compare with Figure 1c), with larger ensemble spread for the historical eruptions (note, SUPER1 consists of only five simulations). HIST1 displays a temporary initial recovery of the temperature signal to within the internal variability range in year 2, when typically a warm ENSO event sets in. The ensemble-mean simulated maximum cooling for HIST1 matches the observed maximum cooling of 0.4 K estimated for the Pinatubo by *Thompson et al.* [2009]. Annual oscillations in the post-eruption anomalous temperature evolution in the ”supervolcano” ensembles indicate a seasonal differentiation of the response, with boreal winter semesters being comparatively colder than summer ones from year 2 onwards. The global temperature responses differ appreciably between SUPER1 and SUPER2. Inter-ensemble differences in global precipitation regard the timing of the post-eruption fluctuation, delayed in the case of SUPER2 compared to SUPER1, rather than the shape of the post-eruption fluctuation and its peak value. Post-eruption anomalies of hemispheric-average surface air temperature (Figure 2c,d) further highlight the differences between historical and “supervolcano” eruptions. For the two historical eruptions, inter-hemispheric differences are small and remain mostly confined within the internal variability range after the first two post-eruption years (Figure 2d). For the “supervolcano” ensembles, inter-hemispheric differences are large and remarkably independent of the location of the eruption (Figure 2d): the Northern Hemisphere undergoes a much stronger and longer lasting cooling compared to the historical ensembles (Figure 2c), with a more pronounced seasonal character than the Southern Hemisphere (compare Figure 2d). As a consequence, in both “supervolcano” ensembles the anomalous hemispheric temperature evolutions deviate considerably from the global estimate.

Overall, we diagnose qualitatively similar features in the different ensembles that point to an amplification of the forced global signals with increased magnitude of the eruption. “Supervolcano” simulations feature a high signal-to-noise ratio, and even the 5-member SUPER1 ensemble is suitable for robust global/hemispheric-scale inferences. Inter-hemispheric differences are apparent in the surface air temperature responses to “supervolcano” but not historical-size eruptions, suggesting that substantially different dynamical responses may characterize the different eruption sizes.

3.2 Sea-ice response

The post-eruption anomalies of Arctic and Antarctic sea-ice area and volume depict major inter-hemispheric differences in the sea-ice responses to both historical and “supervolcano” eruptions (Figure 3). In the Arctic, the total sea ice expands for all eruptions (Figure 3a,c). The post-eruption positive anomalies of total Arctic sea-ice area and volume are of comparable magnitude for the two historical eruptions, but their timing differs. Total Arctic sea-ice area and volume anomalies are about one order of magnitude larger in the “supervolcano” ensembles compared to historical ones. In both ensembles, total sea-ice area and volume entail a sharp increase in simulation years 1 and 2, which is followed by a decadal-scale progressive dampening of the anomaly. The larger anomalies in SUPER2 compared to SUPER1 are likely thermally driven: the volcanic cloud produced by the extra-tropical Yellowstone-like eruption is more confined to the Northern Hemisphere and produces a stronger radiative effect there, i.e. stronger cooling (Figure 2d). The system fully reverts back to within the internal variability range in about 2-2.5 decades.

Significant post-eruption anomalies of Antarctic total sea-ice area and volume (Figure 3b,d) are only detected in the “supervolcano” ensembles. In these ensembles and especially concerning the total sea-ice volume, Antarctic sea-ice anomalies are much smaller than their Arctic counterparts (compare panels c and d of Figure 3). This is true for both the actual anomalies and their values relative to the pre-eruption climatology (which is reported in Figure 3). Initially, a short-lived Antarctic sea-ice area increase occurs approximately within the first two post-eruption years, which is not accompanied by a significant increase in sea-ice volume. This means that, in contrast to the Arctic sea-ice response, there is no post-eruption net build up of Antarctic sea-ice mass. As we will further discuss in section 3.3, the areal expansion likely results in good part from a dynamic response of the Southern Ocean’s sea ice, which is advected over a larger area. This initial expansion phase is followed by a rebound retraction phase of similar amplitude and longer duration (Figure 3b), which is characterized by a drastic reduction in the total sea-ice volume (Figure 3d). Note, reduction in sea-ice volume starts in year 1, when the positive anomaly in sea-ice area is near its peak, meaning that net losses in volume occurs already during the horizontally expanded phase of Antarctic sea ice. In other words, Antarctic sea ice covers a larger area while thinning. This second phase consistently ends about eight years after the eruption. Negative anomalies of both sea-ice area and volume are larger for SUPER1, whose ensemble-spread nonetheless overlaps with that of SUPER2 during the full duration of the rebound fluctuation.

Generally, ensemble-spreads are larger in the Antarctic sea-ice area estimates than in their Arctic counterparts. This is true also for the spread in sea-ice volume in its relative estimates, but not in its absolute values due to smaller Antarctic climatology (Figure 3c,d). Overall, the post-eruption sea-ice evolution appears to be characterized by two distinct phases in the “supervolcano” ensembles: (i) an initial phase of tendential synchronic bi-polar expansion during integration years 1 and 2, and (ii) a subsequent, prolonged phase of inter-hemispheric asymmetry during integration years 4-6.

The anomalies determining the two detected phases of post-eruption sea-ice evolution feature a prominent seasonal character (Figure 4). In the historical ensembles, the significant signals detected in the deseasonalized and smoothed series of total Arctic sea-ice area (Figure 3a) originate from a significant increase during the boreal summer season (Figure 4a). In the “supervolcano” ensembles the initial post-eruption increase in total Arctic sea-ice area occurs throughout the whole year but the magnitude of departures from the climatology is more than doubled in the boreal summer compared to the boreal winter. As we will show in section 3.3, this behavior is most likely due to reduced melting, i.e., thermodynamics is very important for the initial response of Arctic sea ice to volcanic forcing. Predominance of reduced summer melting on winter growth is smeared out in the Arctic delayed response, and the annual cycle averaged over years 4-6 essentially corresponds to an upward-shifted unperturbed annual cycle (Figure 4c). By contrast, the signals in total Antarctic sea-ice area are largest in the sea-ice growth season (Figure 4b), with initial post-eruption gains peaking at ~ 1.9-2.4 million km^2 in June-July and following losses peaking at ~ 1.8-2 million km^2 in August-October (Figure 4d).

Figures 5 and 6 illustrate the regional distribution of sea-ice concentration anomalies for, respectively, the Arctic and the Antarctic region during the two detected phases of post-eruption sea-ice evolution for the SUPER1 ensemble. Mapped values refer to monthly anomalies at the end of the growing season (i.e., March for Arctic sea ice, September for Antarctic sea ice) and of the melting season (i.e., September for Arctic sea ice, March for Antarctic sea ice). Immediately after the eruption, the March Arctic sea-ice concentration increases especially in the gulf of Alaska/eastern Bering Sea and in the outer Labrador Sea/western North Atlantic, where the sea-ice edge significantly advances (Figure 5a). Widespread reduced melting results in extensive increases in September Arctic sea-ice concentrations. These are particularly large in the Canadian Arctic Archipelago and in the Baffin Bay, where the sea-ice edge advances as far as reaching the Hudson and Davis Straits, along the East Greenland current, and in the Barents and Kara Seas, with the latter basin being fully sea-ice covered (Figure 5c). The same regions are important for the total Arctic sea-ice area anomaly in the second phase of the post-eruption areal evolution of sea ice. Then, the strongest contribution to the winter anomaly of Arctic total sea-ice area comes from the North Atlantic/Nordic Seas sector, where March sea-ice concentrations increase by as much as 60% (Figure 5b). September Arctic sea-ice concentration anomalies are also still significant over extensive regions, but with overall smaller amplitudes (Figure 5d).

In the Antarctic, total sea-ice area anomalies are of reduced amplitude and extension in austral summer during both phases (Figure 4b,d). Immediately after the eruption, there is a circumpolar tendency towards positive March anomalies of sea-ice concentration, though these are strongest and most extensive off the West Antarctic coast, where they result in a local advance of the sea-ice edge (Figure 6a). Later on, the same region faces a marked reduction of March sea-ice concentrations and a consequent retreat of the sea-ice edge (Figure 6b), which is again part of a general circumpolar tendency. The regional details of September anomalies of Antarctic sea-ice concentration during the two phases provide a more complex picture (Figure 6c,d). In both phases, negative sea-ice concentration anomalies are diagnosed off the East Antarctic coasts and in the outer Weddell Sea. In the latter region, the response has the typical traits of an open-ocean polynya, i.e. an ice-free area within the ice cover, and is surrounded by positive anomalies leading to a locally advancing sea-ice edge during the initial post-eruption phase (Figure 6c). Anomalies spatially extend more widely in the second phase, when a general retreat of the sea-ice edge is diagnosed (Figure 6d). Whereas no significant large-scale changes are detected west of the Antarctic Peninsula in the initial phase (Figure 6c), the same region faces later a reduction in sea-ice concentration which is locally as large as 60% and results in a strong retreat of the sea-ice edge (Figure 6d). Whereas both phases indicate reductions in September sea-ice concentrations in the outer Ross Sea, the initial post-eruption phase entails also an extensive increase along 60°S (Figure 6c).

Differences between the shown SUPER1 patterns and their SUPER2 analogs (not shown) are generally minor. For historical eruptions, significant post-eruption sea-ice concentration anomalies are usually local, but generally point towards an agreement with the "supervolcano" ensembles concerning the tendencies in the key regions (not shown).

In summary, the sea-ice response to volcanic eruptions in MPI-ESM-COSMOS-Mill strongly depends on the amplitude of the induced global perturbation and, to a lesser extent, the location of the eruption (compare, e.g., the Arctic sea-ice response to the SUPER1/tropical and SUPER2/mid-latitude eruptions). All ensembles feature a temporary post-eruption increase in Arctic sea-ice, while no robust signature on Antarctic sea ice characterizes historical-size eruptions. The post-eruption sea-ice evolution in "supervolcano" simulations can be clearly separated into two phases: an initial one of bi-polar expansion and a delayed one marked by the contrast between persisting Arctic expansion and strong Antarctic contraction. The latter constitutes a counterintuitive simulated behavior, whose explanation seemingly lies in the anomalous seasonal behavior in a few key regions. This is explored further in the next section.

3.3 Mechanism of Arctic and Antarctic sea-ice response to a "supervolcano" eruption

In this section, we focus on the mechanism(s) behind the sea-ice response to the SUPER1 eruption during the initial bi-polar synchronic phase and the subsequent inter-hemispheric asymmetric phase. The SUPER1 ensemble is chosen among the two "supervolcano" eruptions since previous studies on the same ensemble [*Timmreck et al.*, 2010; 2012] provide context to our inferences.

Immediately after the eruption, the meridional air temperature gradient temporarily increases in the lower stratosphere (supplementary Figure S3) due to the in-situ heating by the volcanic aerosols. As a consequence [see, e.g., *Timmreck*, 2012], the stratospheric polar vortex strengthens in both hemispheres until the volcanic cloud dissipates, i.e., for the first two post-eruption years (Figure S4). The tropospheric response is dominated by significant cooling, which persists especially in the Northern

Hemisphere winter (Figure S3), and by weakening of both the Hadley and Ferrell cells (Figures S5-S6), which is consistent with a slow-down of the global hydrological cycle (Figure S7, also compare Figure 2b). The weakening of the general circulation is further associated with weakened tropical and mid-latitude zonal flow in both hemispheres (Figure 7b). This is also concomitant with short-lived anomalous eastward polar circulations, which we interpret as part of the downward propagation of the volcanically-forced strengthened stratospheric polar vortices. Zonal-mean meridional winds at their climatological hemispheric maxima around 30ºN and 50ºS also depict a significant reduction of the zonal-mean northward flow in years 1-2 in the Northern Hemisphere (Figure 7c).

Later on, anomalies in the general atmospheric circulation become less pronounced and are only locally significant, though weaker-than-normal jet conditions remain apparent (Figure S4). So, internal atmospheric processes strongly contribute to the initial response, whereas climatic signals on the decadal scale are mostly related to oceanic and ocean-atmosphere coupled processes. This is for example the case for the significant though rather small increase of the zonal-mean southward flow in years 5-6 detected in the Southern Hemisphere (Figure 7c). The structure of vertical profiles of zonal-mean anomalies of atmospheric parameters depicts an overall symmetry between the general atmospheric circulation of Northern and Southern hemispheres in both phases of post-eruption sea-ice response (Figures S3-S11). The persistent colder tropospheric anomalies over the Arctic, especially during the Northern Hemisphere winter, contrasting the comparatively weak and short-lived Antarctic anomalies represent the most apparent inter-hemispheric asymmetry in the post-eruption atmosphere (Figure S8).

Significant decadal anomalies characterize the post-eruption evolutions of zonal-mean surface temperature and its associated hemispheric meridional gradients (Figure 7a). The post-eruption anomalies depict: (i) strong initial cooling, mostly related to quick responses over the landmasses; (ii) bipolar asymmetry in the form of delayed and prolonged (compared to tropical regions) cooling in the Arctic contrasting the reduced cooling and subsequent warming in the Antarctic; (iii) inter-hemispheric asymmetry in the equator-to-pole temperature gradient, in the form of a temporarily strengthened gradient in the Northern Hemisphere contrasting a prolonged weakened gradient in the

Southern Hemisphere; (iv) delayed (compared to both tropical and polar regions) cooling in the equatorial band, seemingly "phasing" ENSO to a La Niña state in year 3. The latter feature is associated to a temporary reduction of meridional gradients, which feature at this stage highly significant negative anomalies in the Southern Hemisphere.

The anomalous atmospheric energy and oceanic heat transports into the polar regions (Figure 8) provide constraints to our causal interpretation of the diagnosed regional changes. In the Northern Hemisphere, significant (i.e., outside the internal variability range) and prolonged reductions in the meridional heat transport into the Arctic region are diagnosed for both the atmosphere and the ocean: The reduction in atmospheric heat transport peaks at around lag 24-months and remains at significant levels over a 6-year period; oceanic heat transport is reduced below the lower threshold of internal variability around lag 24-months and persists in an anomalously low state for almost one decade. The estimated dry static atmospheric energy transport remains generally within the internal variability range, with a less clear ensemble-mean evolution compared to the moist static energy transport (Figure 8a). This indicates that the latent heat component – entailing reduced global ocean losses to the atmosphere (not shown) and reduced global precipitation (Figure 2b) – dominates the response over the thermal component. At this latitude, the post-eruption anomalous oceanic heat transport is dominated by the gyre component (Figure 8b), which agrees with the general behavior typically simulated by MPI-ESM-COSMOS-Mill [e.g., *Zanchettin et al.*, 2012, 2013a].

In the Southern Hemisphere, the atmospheric energy transport into the Antarctic region is significantly reduced between about 2 and 8 years after the eruption (Figure 8c), reflecting the evolution of anomalous equator-to-pole surface temperature gradient (Figure 7a). In absolute values, the associated peak post-eruption anomaly is about half of its Arctic counterpart (compare panels a and c of Figure 8). An initial, short-lived response is diagnosed in the estimated dry static atmospheric energy transport, compatible with the surface and tropospheric cooling simulated around these latitudes (compare Figure 7a), which is evidently compensated by an increase in the atmospheric latent heat component. Oceanic heat transport into the Antarctic is characterized by strong interannual variability in its post-eruption anomalous evolution as well as by strong internal variability compared to its Arctic counterpart (compare ranges in Figure

8b,d). As a consequence, despite peak anomalies about twice those diagnosed in the Arctic, the post-eruption ocean heat transport into the Antarctic remains mostly within the internal variability range. The most significant feature is a temporary reduction in the total poleward transport around lag of 48 months (Figure 8d). As for the Northern Hemisphere, at these latitudes oceanic transport is dominated by the gyre component.

In summary, both polar regions feature a post-eruption decrease in the energy import. However, the decrease is overall more significant for the Arctic due to an overall more constrained oceanic internal variability range and to constructively superposing and comparable contributions from the atmosphere and the ocean, the former being pivotal in the initial response phase and the latter dominating the response thereafter. For the Antarctic, both oceanic and moist atmospheric energy transports remain initially unaffected, pointing towards dynamical circulation changes as cause for the initial Antarctic sea-ice response. Furthermore, the relevance of the ocean for the post-eruption Antarctic energy budget and its attribution to the imposed forcing is hampered by its strong internal variability. It is therefore important to relate anomalous ocean meridional heat transports to dynamical changes in the oceanic circulation.

In the Northern Hemisphere, the general response of the oceanic circulation to the SUPER1 eruption is in line with the behavior typically simulated by MPI-ESM-COSMOS-Mill after historical-size eruptions [see, e.g., *Zanchettin et al.*, 2012, 2013a]. We therefore only show changes more closely related to sea ice. The post-eruption reduction in gyre-driven northward heat transport is clearly associated with a weakening of the subpolar gyre and of the North Pacific gyre in the Kuroshio-Oyashio extension region (Figure 9a). The weak Gulf Stream together with strong anomalous ocean heat losses to the atmosphere contributes to anomalous cold conditions in the upper polar ocean (not shown). The regional cold anomaly sustains the deepening of the ocean mixed layer, which occurs largely in the western portion of the subpolar gyre and in the Irminger and especially Nordic Seas (Figure 10a). Associated processes of deep water formation result in a progressive intensification of the Atlantic Meridional Overturning Circulation (AMOC) of up to 3 Sv at 30ºN and 1000 m depth, which in turn allows for a delayed temporary increase in the northward ocean heat advection in the tropical and mid-latitude band (not shown). Anomalously strong oceanic convection in the Nordic

Seas occurs also during the second phase of the post-eruption sea-ice response (Figure 10b) due to the persisting cold anomaly (compare Figure 7a). Insulation from the meanwhile advanced sea-ice edge confines the extent of the deepening region (Figure 10b), exemplifying how the sea-ice evolution is fully embedded within the general coupled atmospheric/oceanic response mechanism. We further note that at this later stage, the anomalous patterns of both surface energy fluxes and near-surface atmospheric circulation do not reveal robust large-scale features (not shown), confirming the predominant role (relative to the atmosphere) of the anomalous decadal oceanic evolution for sustaining the post-eruption Arctic sea-ice anomaly.

In the Southern Hemisphere, the initial Antarctic sea-ice response is a dynamical consequence of a strengthened circumpolar westerly circulation along the sea-ice margins. This feature is especially evident in austral winter (Figure 11b), when it describes a poleward shift of the mid-latitude westerlies partly superposing on a positive phase of the Southern Annular Mode. An only similar feature is noticeable in summer, when the pattern describes a weakening of both polar and mid-latitude flow (Figure 11d) typical of a negative phase of the Southern Annular Mode. The marked seasonality in the near-surface wind response goes along with the marked seasonality diagnosed in the sea-ice area response (Figures 4b and 6a,c). Our interpretation is therefore consistent with the enhanced connectivity of observed sea ice variability to the overlying atmospheric circulation associated with large-scale modes like the Southern Annular Mode and ENSO [*Simpkins et al.*, 2012]. Disentangling the different contributions to the post-eruption polar circulation in the southern-hemispheric lower troposphere would require a dedicated study. We only remark the importance of the antagonism between the thermal (i.e., meridional gradient in surface cooling, Figure 7a) and dynamical (i.e., downward propagation of strengthened stratospheric polar vortex) effects. The Antarctic Circumpolar Current (ACC) weakens (Figure 9c) in response to the weakened (in summer) and southward shifted (in winter) circumpolar mid-latitude westerly flow (Figures 7b and 11b,d). During this initial response phase, the ocean undergoes also important dynamical modifications at the regional scale. In particular, the September sea-ice concentration locally decreases in the sea-ice interior region of the outer Weddell Sea (Figure 6c). This area features significantly strengthened ocean energy losses to the atmosphere (Figure 11c) that are related to a significant deepening of the mixed layer (Figure 10c), hence penetration of the post-eruption cold anomaly into the deep ocean layers. Of course, the causal chain linking these features cannot be depicted without the support of dedicated sensitivity experiments. Such response is not diagnosed within the ice-covered region of the Ross Sea despite local strengthening of ocean heat losses (Figure 11c).

Local feedbacks involving sea-ice area, turbulent heat fluxes and modified atmospheric circulation complete the explanation for the diagnosed sea-ice behavior during the second phase of Southern Hemisphere's sea-ice response. We note particularly the anomalous equatorward near-surface atmospheric flows off the West Antarctica coast in austral summer (Figure 12b) and in the outer Ross Sea in austral winter (Figure 12d), which are associated with local negative surface energy flux anomalies over extensive regions (Figure 12a,c). The local anomalous near-surface winds set in under significantly weakened mid-latitude westerly circulation, especially during austral summer (Figure 12b). The anomalous near-surface wind pattern contrasts the zonal-average tendency in the mid-troposphere (Figure 7c) and is consistent with a net reduction of atmospheric energy import into the Antarctic region (Figure 8c). The latter should therefore be regarded as mainly a consequence of local coupled ocean-atmosphere dynamics internal to the Antarctic region. The consistency with corresponding anomalous patterns in the SUPER2 ensemble (not shown) adds support to this interpretation.

Enhanced deep convection still takes place in the Weddell Sea region during the second response phase (Figure 10d), though its magnitude and extent are reduced compared to the initial anomaly. Again, the causal chain for this behavior cannot be fully clarified based on our experiments alone allowing for tentative hypotheses only. We accordingly interpret the strengthened oceanic convection as a likely consequence of locally strengthened surface exchange processes (Figure 12c) favored by the meanwhile decreased winter sea-ice area (Figure 6d). We thus regard the negative sea-ice anomaly as the closure element of the feedback mechanism characterizing the post-eruption ocean-atmosphere evolution in the Weddell Sea region (i.e., the regional anomaly persists until the anomalous large-scale atmospheric circulation sustains a local sea-ice reduction).

4. Summarizing discussion

In this study we used ensemble climate simulations performed with the COSMOS-Mill version of the Max Planck Institute-Earth system model (MPI-ESM) to investigate the decadal response of Arctic and Antarctic sea ice to volcanic perturbations. We considered volcanic eruptions of different magnitude, ranging from historical-size to “supervolcano”-size, the latter with different characteristics, including tropical and extra-tropical locations. In all ensembles a sustained, largely thermally-driven expansion is robustly simulated for total area and volume of Arctic sea ice. Amplitude and duration of the anomalies essentially depend on the magnitude of the imposed forcing. In contrast, the simulated response of Antarctic sea ice is elusive for the historical-size eruptions, while “supervolcano” eruptions induce an initial short-lived, mostly dynamically-driven Antarctic sea-ice expansion which is followed by a prolonged retraction phase. For both historical and “supervolcano” eruption-types we diagnose, therefore, an inter-hemispheric asymmetry in the simulated post-eruption decadal evolution of sea ice.

In the case of a “supervolcano” eruption, the asymmetry primarily derives from the different sensitivity of Arctic and Antarctic regional climates to the induced global energy imbalance and from the associated large-scale atmospheric and oceanic dynamical reactions. Thermodynamics is the key for the Arctic sea-ice expansion, which is triggered by the initially reduced atmospheric heat import and is then sustained on a decadal time scale by the meanwhile reduced oceanic heat import. Noteworthy, decadal responses of North Atlantic/Arctic large-scale oceanic circulation are qualitatively similar for historical and “supervolcano” eruptions, both including a delayed strengthening of the AMOC and a north-westward compression of the subpolar gyre (compare Figure 9b with *Zanchettin et al.* [2012]). For the “supervolcano” eruptions, however, the post-eruption drop in the heat content of the global upper ocean is too large to allow for circulation-driven positive anomalies of ocean heat transport into the Arctic, as diagnosed for historical eruptions [see *Zanchettin et al.*, 2012, 2013a].

In contrast to Arctic sea ice, Antarctic sea ice reacts on the short-term mostly to dynamical atmospheric changes initiated by the volcanically-induced strengthening of the Southern Hemisphere’s stratospheric polar vortex. Antarctic sea ice is thereafter implicated in local surface energy exchange processes dominating the response diagnosed at the hemispheric scale. The post-eruption anomalies of lateral oceanic heat flux are larger in the Antarctic than in the Arctic, but they only temporarily exceed the internal variability range (Figure 8d). We regard the temporarily, significantly decreased poleward oceanic heat transport around year 4 as a marginal contributor to the Antarctic sea-ice anomaly (negative at this stage). Post-eruption negative anomalies of atmospheric energy fluxes are likely a consequence of rather than a cause of the chain of local feedbacks within the Antarctic region. The substantially different exposure of the Arctic and Antarctic regional climates to volcanically-forced energy imbalances explains why the inter-hemispheric asymmetry becomes apparent with increasing magnitude of the eruption.

In both the Arctic and the Antarctic, regions of strongest simulated sea-ice response correspond to key regions for sea-ice and ice-cap variability found in reconstructions and observations. For instance, extensive increases in September Arctic sea-ice concentrations are simulated in the Canadian Arctic Archipelago and in the Baffin Bay (Figure 5c). This is in agreement with records of ice-cap growth from Arctic Canada covering the last millennium indicating a strong link to large volcanic eruptions [*Anderson et al.*, 2008; *Miller et al.*, 2012]. In our simulations, internal variability of Antarctic sea ice is stronger for total area and weaker for total volume compared to Arctic sea ice (Figure 3, note that total Antarctic sea-ice volume is almost half its Arctic counterpart). As shown by the forced responses, hemispheric metrics for the Antarctic often mask strong spatially-heterogeneous variability (Figure 6c), as also indicated by observations [e.g., *Simpkins et al.*, 2012, 2013]. The interplay between large-scale dynamics and local processes highlights several relevant mechanisms and features, which need to be reliably represented in models to build confidence in the simulated representation of post-eruption sea-ice evolutions, particularly for the Antarctic. These include, among others, the global hydrological cycle, the downward propagation of polar vortex signals, ENSO, the global oceanic conveyor of heat, and the atmospheric forcing of the Antarctic circumpolar current (ACC).

The downward propagation of volcanically-forced stratospheric signals, especially the post-eruption strengthening of the stratospheric polar vortex, is important for the initial dynamical atmospheric response to explosive volcanic eruptions [e.g., *Stenchikov et al.*, 2006; *Fischer et al.*, 2007; *Zanchettin et al.*, 2012]. The stratospheric polar vortex significantly strengthens after the eruption in both hemispheres in HIST2, SUPER1 (Figure S4) and SUPER2, with duration tracing that of the imposed radiative anomaly, but it does not in HIST1 (not shown). Signals in the polar mid-troposphere are robust only for "supervolcano" eruptions (compare Figure 7b). Larger ensembles could fully clarify whether the lack of robust dynamical atmospheric responses for historical eruptions reflects a low signal-to-noise ratio rather than a truly lacking dynamical response. The latter hypothesis, however, is supported by the deficient representation of stratospheric dynamics and stratospheric-tropospheric coupling in latest-generation "low-top" coupled general circulation models (CGCMs) [*Charlton-Perez et al.*, 2013; *Omrani et al*., 2013], a characteristic which is shared by the version of MPI-ESM used here.

Similar concerns arise about the simulated southern tropospheric mid-latitude jet, e.g., its too equatorward climatological position [e.g., *Swart and Fyfe*, 2012]. Furthermore, simulated Antarctic sea-ice variability and sensitivity to external disturbances may as well suffer from an imperfect description of tropospheric internal dynamics, e.g., those related to variability of the Southern Annular Mode [*Simpson et al.*, 2012] and of the associated surface wind variability [*Zhang*, 2013]. In particular, the strength and latitudinal position of the circumpolar winds affect the Antarctic sea ice via the Ekman transport [*Maksym et al.*, 2012; *Landrum et al.*, 2012; *Weijer et al.*, 2012]. In our simulations the total Antarctic sea-ice volume does not support the early post-eruption horizontal expansion phase (Figure 3b,d) leading to sea-ice thinning. This contrasts other model-based indications that wind intensification tends to increase Antarctic sea-ice volume through increased ridged ice production [*Zhang*, 2013]. The post-eruption initial resilience of total Antarctic sea-ice volume may therefore reflect a truly distinct dynamical behavior related to extremely strong volcanic forcing, but it may also reflect poor representation of near-surface atmospheric circulation. This is important for the case discussed here, given also the marked seasonal character of Antarctic sea-ice response to the volcanic perturbation during the delayed contraction phase (Figure 4d).

The timing of the strongest post-eruption surface cooling at equatorial latitudes, delayed with respect to that at mid-latitudes strongly contributes to the post-eruption strengthening of meridional gradients (Figure 7). This equatorial cooling has a strong imprint in the Pacific in the form of an apparent phasing of ENSO on a delayed La Niña state. This robust response of ENSO to the volcanic perturbation occurs after the maximum global surface cooling (compare with Figure 2a), when the Toba/SUPER1 ensemble indicates a non-significant, though tendentially warm, ENSO response [*Timmreck et al.*, 2010]. ENSO in this version of MPI-ESM was consistently found to be only weakly sensitive to volcanic forcing for a selection of historical-size eruptions in transient climate simulations covering the last millennium, with an only tendential response towards a cold (La Niña) anomaly [*Zanchettin et al.*, 2012]. Nonetheless, two considerations limit our confidence on the simulated forced behavior of ENSO. First, ENSO's representation still is a challenge for coupled climate models [e.g., *Guilyardi et al.*, 2009] and MPI-ESM-COSMOS-Mill produces too strong and too regular ENSO fluctuations [compare *Jungclaus et al.*, 2006]. Second, while observations are still insufficient to draw confident conclusions about the role of ENSO for post-eruption dynamics of tropical and extra-tropical climates, a recent reconstruction points to a robust ENSO response to the largest historical tropical eruptions consisting of immediate cooling followed by anomalous warming one year after [*Li et al.*, 2013]. The disagreement between indications from this paleoclimate record and from MPI-ESM-COSMOS-Mill simulations asks for additional dynamical investigations that are beyond the scope of this study.

The strength of the ACC is overestimated in MPI-ESM-COSMOS-Mill [*Marsland et al.*, 2003; compare also: *Jungclaus et al.*, 2013]. Implications for the diagnosed post-eruption Antarctic sea-ice evolutions and for the global redistribution of ocean heat anomalies are difficult to disentangle without dedicated sensitivity experiments. We note, however, that an overly strong and displaced ACC corresponds to a biased structure and strength of the subpolar gyres and of associated oceanic convective activity. In fact, the ocean model MPIOM largely overestimates the mixed layer depth in the Ross Sea and Weddell Sea gyres [*Griffies et al*., 2009]. The latter is associated with the occurrence of a small permanent polynya [*Marsland et al.*, 2003]. Biases of this kind could be relevant for the delayed reduction diagnosed in Antarctic sea ice (Figure 6d) as well as for the propagation of heat anomalies into the deep ocean (Figure 11c,d). As shown by different models, ocean/sea-ice mechanisms during the sea-ice growth phase are strongly interrelated with oceanic stratification and ocean vertical heat transport. In a weakly stratified Southern Ocean, ice melting from ocean heat flux decreases faster than the ice growth, leading to an increase in the net ice production and hence an increase in ice mass [*Zhang*, 2007]. In the Community Climate System Model version 3, the freshwater flux between Antarctic sea ice and the Southern Ocean is closely intertwined with ocean convection and deep-ocean heat uptake [*Kirkman and Bitz*, 2011]. On the one hand, a (climatologically) excessively mixed Southern Ocean, as in MPIOM [*Griffies et al*., 2009], implies reduced efficiency of external forcings to produce anomalous heat fluxes. On the other hand, locally excessive convective strength as in the Weddell Sea would imply enhanced oceanic heat losses to the atmosphere. Consequently, simulated estimates of post-eruption global air-surface cooling [e.g., *Timmreck et al.*, 2010] may be biased towards being too conservative.

A linkage exists between internally-generated multidecadal- and centennial-scale variability of the Weddell Sea sea-ice cover and of the AMOC in the Kiel Climate Model [*Park and Latif*, 2008], where oceanic deep convection within the Weddell Sea gyre plays a central role in the inter-hemispheric connection [*Martin et al.*, 2013]. Ascribing a similar bipolar ocean seesaw to the decadal-scale volcanically-forced evolutions presented here, one would expect that the enhanced deep convection in the Weddell Sea (Figure 11c,d) hampers the southward deep water flow in the North Atlantic, i.e., promote an AMOC slow-down. Overly-strong ocean convection in the Weddell Sea could accordingly help explain the overall weaker post-eruption AMOC strengthening in MPI-ESM-COSMOS-Mill compared to other CGCMs, as discussed in *Zanchettin et al.* [2012]. We note nonetheless that this has likely only faint implications for the post-eruption decadal Arctic sea-ice evolution, since the northward oceanic heat transport at subpolar and polar latitudes is largely determined by the gyre circulation (Figure 8b, see also *Zanchettin et al.*, 2012, 2013a).

Perturbation experiments like the described “supervolcano” experiments highlight known limits and less understood features of CGCMs and Earth system models, and might therefore help to delimit the reliability of their forced dynamical climate responses in more general contexts. We foresee several advantages in a more extensive employment of “supervolcano” simulations as analog of, e.g., sudden warming experiments. The restoration from the induced cold anomaly highlights variability modes and teleconnections that would arise under background warming conditions due predominantly to internal climate variability, whereas externally-forced warming experiments produce forced anomalous patterns of climate variability. We remark that our 5-member Toba simulation ensemble was sufficient to yield largely significant, hence coherent, dynamical responses. Thus, such a small-size ensemble allows for confident inferences about simulated forced global [*Timmreck et al.*, 2010] as well as regional [*Timmreck et al.*, 2012] changes. As shown here, "supervolcano" experiments allow gaining insights on the relative importance of the thermodynamical and dynamical components of sea-ice responses to imposed negative net radiative imbalances. Such separation highlights differences in the internal hemispheric dynamics related to external radiative perturbations.

5. Conclusions

Ensemble Earth-system-model simulations depict inter-hemispheric differences in the decadal sea-ice response to strong volcanic eruptions regarding both the sensitivity to the forcing and the sign of the induced anomalies. Arctic sea ice is very sensitive to volcanic forcing owing especially to its strong exposure to externally-forced changes in meridional heat transport. By contrast, Antarctic sea ice appears to be less susceptible to volcanic forcing and responds only to extremely large (so-called "supervolcano") eruptions. In further contrast to Arctic sea ice, the post-eruption evolution of Antarctic sea ice is mostly determined by feedbacks that set in within the Antarctic region. Whereas Arctic sea ice robustly expands for a prolonged period after major volcanic eruptions, the post-eruption Antarctic sea ice evolution includes an initial short-lived expansion and a subsequent prolonged contraction phase. This sea-ice asymmetry reflects the potential of volcanic forcing to significantly affect inter-hemispheric interannual-to-decadal climate variability in a broader context. Nonetheless, key processes implied in the generation of the asymmetry include less understood, hence poorly simulated features. This poses non-negligible caveats when extrapolating simulation-based inferences to the real climate system. In this sense, idealized "supervolcano" perturbation experiments could serve the assessment of climate models' performances under strong forcing conditions.

Acknowledgements

The authors thank Achim Stössel for the helpful discussions and comments on an earlier version of the manuscript, and Kay Hübner for the motivating initial analyses. Comments from two anonymous reviewers helped improving the clarity of the manuscript. This work benefitted from the MPI-M integrated projects ‘‘Millennium’’ and ‘‘Super Volcano’’. This work was supported by the Federal Ministry for Education and Research in Germany (BMBF) through the research program "MiKlip" (FKZ:01LP1158A(DZ):/01LP1130A(CT)).

References

Ahmed, M., et al. (2013) Continental-scale temperature variability during the past two millennia. Nat. Geosc., 6, 339-346, doi:10.1038/NGEO1797

Anderson, R. K., Miller, G. H., Briner, J. P., Lifton, N. A., and S. B. DeVogel (2008), A millennial perspective on Arctic warming from 14C in quartz and plants emerging from beneath ice caps. Geophys. Res. Lett. 35:L01502, doi:10.1029/2007GL032057

Barlyaeva, T. V., I. A. Mironova, and D. I. Ponyavin (2009), Nature of decadal variations in the climatic data of the second half of the 20th century. Dokl. Earth. Sci. 425A(3):419–423

Beitsch, A., J. H. Jungclaus, and D. Zanchettin (2013) Patterns of decadal-scale Arctic warming events in simulated climate. Clim. Dyn. doi:10.1007/s00382-013-2004-5

Bitz, C.M., and L.M. Polvani (2012), Antarctic climate response to stratospheric ozone depletion in a fine resolution ocean climate model, Geophys. Res. Lett., 39, L20705, doi:10.1029/2012GL053393

Bothe, O., J. H. Jungclaus, D. Zanchettin, and E. Zorita (2013) Climate of the last millennium: ensemble consistency of simulations and reconstructions. Clim. Past, 9, 1089–1110, doi:10.5194/cp-9-1-2013

Brohan P, Kennedy JJ, Harris I, Tett SFB, Jones PD (2006) Uncertainty estimates in regional and global observed temperature changes: a new dataset from 1850. J. Geophys. Res. 111:D12106, doi:12110.11029/12005JD006548

Charlton-Perez, A. J., et al. (2013), On the lack of stratospheric dynamical variability in low-top versions of the CMIP5 models. J. Geophys. Res., 118, 2494–2505, doi:10.1002/jgrd.50125

Chylek, P., Folland, C.K., Lesins, G., and M. K. Dubey (2010) Twentieth century bipolar seesaw of the Arctic and Antarctic surface air temperatures. Geophys. Res. Lett. 37, L08703, doi:10.1029/2010GL042793

Crowley, T. J., and M. B. Unterman (2012) Technical details concerning development of a 1200-yr proxy index for global volcanism, Earth Syst. Sci. Data Discuss., 5, 1-28, doi:10.5194/essdd-5-1-2012

Crowley, T. J., et al. (2008), Volcanism and the little ice age, PAGES News, 16:22–23

Duncan, R. P., P. Fenwick, J. G. Palmer, M. S. McGlone, and C. S. M. Turney (2010) Non-uniform interhemispheric temperature trends over the past 550 years. Clim. Dyn. 35:1429–1438, doi:10.1007/s00382-010-0794-2

Fernández-Donado, L., and co-authors (2013) Large-scale temperature response to external forcing in simulations and reconstructions of the last millennium. Clim. Past, 9, 393–421, doi:10.5194/cp-9-393-2013

Fischer, E., J. Luterbacher, E. Zorita, S. F. B. Tett, C. Casty, and H. Wanner (2007), European climate response to tropical volcanic eruptions over the last half millennium, Geophys. Res. Lett., 34, L05707, doi:10.1029/2006GL027992

Gillett, N. P., and D. W. J. Thompson (2003) Simulation of Recent Southern Hemisphere Climate Change. Science, 302 (5643), 273-275, doi:10.1126/science.1087440

Graf, H.F., and D. Zanchettin (2012), Central Pacific El Niño, the ‘‘subtropical bridge’’ and Eurasian Climate. J. Geophys. Res., 117, D01102, doi:10.1029/2011JD016493

Griffies, S. M., et al. (2009), Coordinated Ocean-ice Reference Experiments (COREs). Oce. Modelling, 26: 1–46, doi:http://dx.doi.org/10.1016/j.ocemod.2008.08.007

Guilyardi, E., A. Wittenberg, A. Fedorov, M. Collins, C.Z. Wang, A. Capotondi, G.J. van Oldenborgh, and T. Stockdale (2009) Understanding El Niño in ocean-atmosphere General Circulation Models: Progress and challenges. Bull. Amer. Met. Soc., 90, 325–340

Henriksson, S.V. , P. Räisänen, J. Silén, and A. Laaksonen (2012) Quasiperiodic climate variability with a period of 50-80 years: Fourier analysis of measurements and Earth System Model simulations. Clim. Dyn. 39: 7-8, 1999-2011, doi:10.1007/s00382-012-1341-0

Heuzé, C., K. J. Heywood, D. P. Stevens, and J. K. Ridley (2013) Southern Ocean bottom water characteristics in CMIP5 models. Geophys. Res. Lett., 40, 1409–1414, doi:10.1002/grl.50287

Holden, P. B. N. R. Edwards, E.W. Wolff, N. J. Lang, J. S. Singarayer, P. J. Valdes, and T. F. Stocker (2010) Interhemispheric coupling, the West Antarctic Ice Sheet and warm Antarctic interglacials. Clim. Past, 6, 431-443, doi:10.5194/cp-6-431-2010

Jones, G. S., J. M. Gregory, P. A. Stott, S. F. B. Tett, and R. B. Thorpe (2005) An AOGCM simulation of the climate response to a volcanic super-eruption. Clim. Dyn. 25, 725-738

Jungclaus J.H., N. Keenlyside, M. Botzet, H. Haak, J. J. Luo, M. Latif, J. Marotzke, U. Mikolajewicz, and F. Roeckner (2006) Ocean circulation and tropical variability in the coupled model ECHAM5/MPI-OM. J Clim 19:3952–3972

Jungclaus, J. H., et al. (2010), Climate and carbon-cycle variability over the Last Millennium. Clim. Past, 6, 723-737, doi:10.5194/cp-6-723-2010

Jungclaus J. H., et al. (2013) Characteristics of the ocean simulations in MPIOM, the ocean component of the Max Planck Institute Earth System Model. J. Adv. Model. Earth Syst., doi:10.1002/jame.20023

Karpechko, A. Y., N. P. Gillett, M. Dall'Amico, and L. J. Gray (2010), Southern Hemisphere atmospheric circulation response to the El Chichón and Pinatubo eruptions in coupled climate models, Q. J. R. Meteorol. Soc., 136, 1813-1822, doi:10.1002/qj.683

Keith, D.W. (1995) Meridional energy transport: uncertainty in zonal means. Tellus, 47A, 30-44

King, J. (2014) Climate science: A resolution of the Antarctic paradox. Nature 505, 491–492, doi:10.1038/505491a

Kinnard, G., Zdanowicz, C.M., Fisher, D.A., Isakkson, E., de Vernal, A., Thompson, L.G. (2011) Reconstructed changes in Arctic sea ice over the past 1,450 years. Nature 479: 509-513, doi:10.1038/nature10581

Kirkman, C. and C.M. Bitz (2011), The Effect of the Sea Ice Freshwater Flux on Southern Ocean Temperatures in CCSM3: Deep Ocean Warming and Delayed Surface Warming, J. Climate, 24, pp. 2224-2237 doi: 10.1175/2010JCLI3625

Koldunov, N. V., D. Stammer, and J. Marotzke (2010) Present-Day Arctic Sea Ice Variability in the Coupled ECHAM5/MPI-OM Model. J. Climate, 23, 2520–2543. doi:http://dx.doi.org/10.1175/2009JCLI3065.1

Landrum, L., M. M. Holland, D. P. Schneider, and E. Hunke (2012) Antarctic Sea Ice Climatology, Variability, and Late Twentieth-Century Change in CCSM4. J. Clim.25, 4817-4838, doi:10.1175/JCLI-D-11-00289.1

Li, C., D. Notz, S. Tietsche, and J. Marotzke (2013) The Transient versus the Equilibrium Response of Sea Ice to Global Warming. J. Climate, 26, 5624–5636. doi: http://dx.doi.org/10.1175/JCLI-D-12-00492.1

Li, J., S.-P. Xie, E. R. Cook, M. S. Morales, D. A. Christie, N. C. Johnson, F. Chen, R. D’Arrigo, A. M. Fowler, X. Gou, and K. Fang. (2013) El Niño modulations over the past seven centuries. Nature Cl. Ch., 3:9, 822-826, doi:10.1038/NCLIMATE1936

Maksym, T., S.E. Stammerjohn, S. Ackley, and R. Massom (2012) Antarctic sea ice—A polar opposite? *Oceanography* 25(3):140–151, http://dx.doi.org/10.5670/oceanog.2012.88.

Marshall, G.J., (2003) Trends in the Southern Annular Mode from observations and reanalyses. J. Clim., 16:4,134–4,143, http://dx.doi.org/10.1175/1520-0442(2003)016<4134:TITSAM>2.0.CO;2

Marsland, S.J., H. Haak, J.H. Jungclaus, M. Latif, and F. Röske (2003), The Max Planck Institute global ocean/sea ice model with orthogonal curvilinear coordinates, *Ocean Modell.*, *5*, 91-127

Martin, T., W. Park, and M. Latif (2013) Multi-centennial variability controlled by Southern Ocean convection in the Kiel Climate Model. Clim. Dyn., 40:2005–2022, doi:10.1007/s00382-012-1586-7

Massonnet, F., P. Mathiot, T. Fichefet, H. Goosse, C. K. Beatty, M. Vancoppenolle, and T. Lavergne (2013), Model reconstruction of the Antarctic sea ice thickness and volume changes over 1980–2008 using data assimilation. Oce. Modelling, 64: 67-75, http://dx.doi.org/10.1016/j.ocemod.2013.01.003

Meier, W. N., D. Gallaher, and G. G. Campbell (2013), New estimates of Arctic and Antarctic sea ice extent during September 1964 from recovered Nimbus I satellite imagery. Cryosph., 7:699-705, doi:10.5194/tc-7-699-2013

Menary, M.B., W. Park, K. Lohmann, M. Vellinga, M.D. Palmer, M. Latif, and J.H. Jungclaus (2012) A multimodel comparison of centennial Atlantic meridional overturning circulation variability. Clim. Dyn. 38:11-12, 2377-2388

Miller, G. H., et al. (2012), Abrupt onset of the Little Ice Age triggered by volcanism and sustained by sea-ice/ocean feedbacks, Geophys. Res. Lett., 39, L02708, doi:10.1029/2011GL050168

Niemeier, U., et al. (2009), Initial fate of fine ash and sulfur from large volcanic eruptions, Atmos. Chem. Phys., 9, 9043–9057

Notz, D., and J. Marotzke (2012) Observations reveal external driver for Arctic sea-ice retreat. Geophys. Res. Lett. 39(8), doi:10.1029/2012GL051094

Omrani, N.-E., Keenlyside, N., Bader, J., & Manzini, E. (2013). Stratosphere key for wintertime atmospheric response to warm Atlantic decadal conditions. *Clim. Dyn.*, doi:10.1007/s00382-013-1860-3

Park, W., and M. Latif (2008), Multidecadal and multicentennial variability of the meridional overturning circulation. Geophys. Res. Lett. 35:L22703, doi:10.1029/2008GL035779

Parkinson, C. L. (2004) Southern Ocean sea ice and its wider linkages: insights revealed from models and observations. Antarctic Science 16 (4): 387–400, doi:10.1017/S0954102004002214

Polvani, L. M., and K. L. Smith (2013) Can natural variability explain observed Antarctic sea ice trends? New modeling evidence from CMIP5. Geophys. Res. Lett. 40, 3195–3199, doi:10.1002/grl.50578

Raddatz, T.J., et al (2007), Will the tropical land biosphere dominate the climate-carbon cycle feedback during the twenty-first century? Clim Dyn 29:565–574

Robock, A., T. Adams, M. Moore, L. Oman, and G. Stenchikov (2007) Southern Hemisphere atmospheric circulation effects of the 1991 Mount Pinatubo eruption, Geophys. Res. Lett. 34, doi:10.1029/2007GL031403

Roeckner, E., et al. (2006), Sensitivity of simulated climate to horizontal and vertical resolution in the ECHAM5 atmosphere model, J. Clim., 19, 3771–3791, doi:http://dx.doi.org/10.1175/JCLI3824.1

Russell, J. L., R. J. Stouffer, and K. W. Dixon (2006) Intercomparison of the Southern Ocean Circulations in IPCC Coupled Model Control Simulations, J. Clim. 19:4560-4575

Sallée, J.-B., E. Shuckburgh, N. Bruneau, A. J. S. Meijers, T. J. Bracegirdle, and Z. Wang (2013), Assessment of Southern Ocean mixed layer depths in CMIP5 models: Historical bias and forcing response, J. Geophys. Res. Oceans, 118, 1845–1862, doi:10.1002/jgrc.20157

Schaefer, J.M., Denton, G.D., Kaplan, M.R., et al. (2009) High-frequency Holocene glacier fluctuations in New Zealand differ from the northern signature. Science 324: 622–625

Schleussner, C. F., and G. Feulner (2012) A volcanically triggered regime shift in the subpolar North Atlantic ocean as a possible origin of the Little Ice Age. Clim. Past Discuss., 8, 6199–6219, doi:10.5194/cpd-8-6199-2012

Schubert, J. J., B. Stevens, T. Crueger. (2013) Madden-Julian oscillation as simulated by the MPI Earth System Model: Over the last and into the next millennium. J. Adv. Model. Earth Sys., 5:1, 71-84, doi:10.1029/2012MS000180

Segschneider J., A. Beitsch, C. Timmreck, V. Brovkin, T. Ilyina, J. Jungclaus, S. J. Lorenz, K. D. Six, and D. Zanchettin (2013) Impact of an extremely large magnitude volcanic eruption on the global climate and carbon cycle estimated from ensemble Earth System Model simulations. Biogeosc. 10, 669–687, doi:10.5194/bg-10-669-2013

Shakun, J.D., et al. (2012) Global warming preceded by increasing carbon dioxide concentrations during the last deglaciation, Nature 484, 49–54, doi:10.1038/nature10915

Shin, S.-I., Z. Liu, B. L. Otto-Bliesner, J. E. Kutzbach, and S. J. Vavrus (2003) Southern Ocean sea-ice control of the glacial North Atlantic thermohaline circulation. Geophys. Res. Lett. 30(2), 1096, doi:10.1029/2002GL015513

Sigmond, M., and J. C. Fyfe (2014) The Antarctic Sea Ice Response to the Ozone Hole in Climate Models. J. Climate, 27, 1336–1342, doi: http://dx.doi.org/10.1175/JCLI-D-13-00590.1

Simpkins, G. R., L. M. Ciasto, D. W. J. Thompson, and M. H. England (2012) Seasonal Relationships between Large-Scale Climate Variability and Antarctic Sea Ice Concentration. J. Climate, 25, 5451–5469, doi: http://dx.doi.org/10.1175/JCLI-D-11-00367.1

Simpkins,G. R., L. M. Ciasto, and M. H. England (2013) Observed variations in multidecadal Antarctic sea ice trends during 1979–2012, Geophys. Res. Lett. 40, 1–6, doi:10.1002/grl.50715

Simpson, I., P. Hitchcock, T. Shepherd, and J. Scinocca (2012) Southern Annular Mode Dynamics in Observations and Models. Part 1: the Influence of Climatological Zonal Wind Biases in a Comprehensive GCM. J. Climate, doi:10.1175/JCLI-D-12-00348.1, in press

Stammerjohn, S., R. Massom, D. Rind, and D. Martinson (2012), Regions of rapid sea ice change: An inter-hemispheric seasonal comparison. *Geophys. Res. Lett.*, 39, L06501, doi:10.1029/2012GL050874

Stenchikov, G., K. Hamilton, R. J. Stouffer, A. Robock, V. Ramaswamy, B. Santer, and H.-F. Graf (2006), Arctic Oscillation response to volcanic eruptions in the IPCC AR4 climate models, J. Geophys. Res., 111, D07107, doi:10.1029/2005JD006286

Stenchikov, G., T. L.Delworth,V. Ramaswamy, R. J. Stouffer, A.Wittenberg, and F. Zeng (2009), Volcanic signals in oceans, J. Geophys. Res., 114, D16104, doi:10.1029/2008JD011673

Stier, P., et al. (2005), The aerosol climate model ECHAM5□HAM, Atmos. Chem. Phys., 5, 1125–1156

Stössel, A., Zhang, Z., and Vihma, T. (2011) The effect of alternative real-time wind forcing on Southern Ocean sea-ice simulations. J.Geophys.Res.116, C11021, doi:10.1029/2011JC007328

Stouffer, R. J., and Coauthors (2006), GFDL's CM2 Global Coupled Climate Models. Part IV: Idealized Climate Response. J. Clim., 19, 723–740, doi:http://dx.doi.org/10.1175/JCLI3632.1

Stroeve, J. C., V. Kattsov, A. P. Barrett, M. C. Serreze, T. Pavlova, M. M. Holland, and W. N. Meier (2012), Trends in Arctic sea ice extent from CMIP5, CMIP3 and observations, *Geophys. Res. Lett.*, 39(16), L16502, doi:10.1029/2012GL052676

Swart, N. C., and J. C. Fyfe (2012) Observed and simulated changes in southern hemisphere surface westerlies. Geophys. Res. Lett., 39, L16 711, doi:10.1029/2012GL052810

Thompson, D. W. J., J. M. Wallace, P. D. Jones, and J. J. Kennedy (2009) Identifying Signatures of Natural Climate Variability in Time Series of Global-Mean Surface Temperature: Methodology and Insights. *J. Climate*, **22**, 6120–6141.

Tietsche, S., D. Notz,, J. H. Jungclaus and J. Marotzke (2011) Recovery mechanisms of Arctic summer sea ice. Geophys. Res. Lett., 38, L02707, doi:10.1029/2010GL045698

Timmreck, C., S. J. Lorenz, T. J. Crowley, S. Kinne, T. J. Raddatz, M. A. Thomas, and J. H. Jungclaus (2009), Limited temperature response to the very large AD 1258 volcanic eruption, Geophys. Res. Lett., 36, L21708, doi:10.1029/2009GL040083.

Timmreck, C., H.-F. Graf, S. J. Lorenz, U. Niemeier, D. Zanchettin, D. Matei, J. H. Jungclaus and T.J. Crowley (2010), Aerosol size confines climate response to volcanic super-eruptions, Geophys. Res. Lett. 37, L24705, doi:10.1029/2010GL045464.

Timmreck, C. (2012), Modeling the climatic effects of large volcanic eruptions. WIREs Clim. Change, 3, 545–564, doi:10.1002/wcc.192

Timmreck C, H.-F. Graf, D. Zanchettin, S. Hagemann, T. Kleinen and K. Krüger (2012) Climate response to the Toba eruption: regional changes. Quat Int. 258,30-44.

Turner, J., J. C. Comiso, G. J. Marshall, T. A. Lachlan-Cope, T. Bracegirdle, T. Maksym, M. P. Meredith, Z. Wang, and A. Orr (2009) Non-annular atmospheric circulation change induced by stratospheric ozone depletion and its role in the recent increase of Antarctic sea ice extent. Geophys. Res. Lett., 36, L08502, doi:10.1029/2009GL037524

Turner, J., T. Bracegirdle, T. Phillips, G. J. Marshall, and J. S. Hosking (2013), An Initial Assessment of Antarctic Sea Ice Extent in the CMIP5 Models. J. Climate, 26, 1473–1484, doi:http://dx.doi.org/10.1175/JCLI-D-12-00068.1

Wang, M. and J. E. E. Overland (2012) A sea ice free summer Arctic within 30 years-an update from CMIP5 models, *Geophys. Res. Lett.*, doi:10.1029/2012GL052868, in press

Weber, M. E., P. U. Clark, W. Ricken, J. X. Mitrovica, S. W. Hostetler, and G. Kuhn (2011) Interhemispheric Ice-Sheet Synchronicity During the Last Glacial Maximum. Science, 334(6060), 1265-1269, doi:10.1126/science.1209299

Weijer, W., et al. (2012) The Southern Ocean and its climate in CCSM4. J. Climate, 25, 2652–2675, doi:10.1175/JCLI-D-11-00302.1

Wetzel, P., Winguth, A., and E. Maier-Reimer (2005), Sea-to-air CO2 fluxes from 1948 to 2003. Glob Biogeochem Cycles 19 GB2005. doi:10.1029/2004GB002339

Zanchettin, D., C. Timmreck, H.-F. Graf, A. Rubino, S. Lorenz, K. Lohmann, K. Krueger, and J. H. Jungclaus (2012), Bi-decadal variability excited in the coupled ocean–atmosphere system by strong tropical volcanic eruptions. Clim. Dyn., 39:1-2, 419-444, DOI:10.1007/s00382-011-1167-1

Zanchettin, D., O. Bothe, H. F. Graf, S. J. Lorenz, J. Luterbacher, C. Timmreck, and J. H. Jungclaus (2013a) Background conditions influence the decadal climate response to strong volcanic eruptions. J. Geophys. Res. Atm., 118(10): 4090-4106, doi:10.1002/jgrd.50229

Zanchettin, D., A. Rubino, D. Matei, O. Bothe, and J. H. Jungclaus (2013b) Multidecadal-to-centennial SST variability in the MPI-ESM simulation ensemble for the last millennium. Clim. Dyn., 40:5, 1301-1318, doi:10.1007/s00382-012-1361-9

Zhang, J. (2007) Increasing Antarctic Sea Ice under Warming Atmospheric and Oceanic Conditions, J. Climate, 20, 2515–2529, doi: http://dx.doi.org/10.1175/JCLI4136.1

Zhang, J. (2013) Modeling the impact of wind intensification on Antarctic sea ice volume. J. Clim., doi: http://dx.doi.org/10.1175/JCLI-D-12-00139.1

Zhong, Y., et al (2011) Centennial-scale climate change from decadally-paced explosive volcanism: a coupled sea ice-ocean mechanism. Clim Dyn 37:11-12, 2373-2387, doi:10.1007/s00382-010-0967-z

Figure captions

Figure 1 – Simulated imposed forcing in the two historical and the two “supervolcano” ensembles as diagnosed through anomalies in the global-average top-of-atmosphere solar (shortwave, a), thermal (longwave, b) and net (c) radiation. Lines (shading): mean (standard error of the mean). Black dotted lines indicate the internal variability range (*n*=10, see methods). The magenta vertical hatched line indicates the approximate start of the eruptions. Lag(0) corresponds to January of the eruption year. Positive anomalies correspond to increased downward flux. No smoothing was applied to the series.

Figure 2 – Simulated post-eruption anomalies of global-average surface (2 meters) air temperature (SAT) (panel a) and total precipitation (b), and Northern-hemispheric average SAT (c) and difference between Northern and Southern-hemispheric average SAT (d) for the two historical and the two “supervolcano” ensembles. Lines (shading): mean (standard error of the mean). Black dashed lines indicate the internal variability range (*n*=10, see methods). The magenta vertical hatched line indicates the approximate start of the eruptions. Lag(0) corresponds to January of the eruption year. Note that the y-axis in panels c and d has the same scale, highlighting the relative magnitude of inter-hemispheric differences in the temperature response.

Figure 3 – Simulated post-eruption anomalies of Arctic (top) and Antarctic (bottom) total sea-ice area (top panels) and volume (bottom) for the two historical and the two “supervolcano” ensembles. Lines (shading): mean anomaly (standard error of the mean). Anomalies are smoothed with a 13-months centered moving average. Black dashed lines

indicate the internal variability range (*n*=10¸ see methods). The magenta vertical hatched line indicates the approximate start of the eruptions. Lag(0) corresponds to January of the eruption year. The number on top-right of each panel is the approximate pre-eruption climatology. The y-axis has the same scale in panels a and b, and in panels c and d, highlighting the different magnitude of the hemispheric responses.

Figure 4 – Ensemble-mean simulated seasonal evolutions of hemispheric sea-ice area for integration years 1-2 (panels a, b) and 4-6 (panels c,d) for the two historical and the two “supervolcano” ensembles. Gray shading (hatched white line) represents the 98% range (mean) for signal occurrence in the control run. Signal in the control run corresponds to the annual evolution averaged over three randomly chosen consecutive years, for a 10-member ensemble.

Figure 5 – Ensemble-mean simulated March (top panels) and September (bottom panels) Arctic sea-ice concentration anomalies for integration years 1-2 (panels a, b) and 4-6 (panels c,d) of the SUPER1 ensemble. Only grid points where the anomaly is significant at 95% confidence (*n*=5, see methods) are shown. The green and orange lines indicate, respectively, the pre-eruption average and post-eruption average sea-ice edge.

Figure 6 – Ensemble-mean simulated March (top panels) and September (bottom panels) Antarctic sea-ice concentration anomalies for integration years 1-2 (panels a, b) and 4-6 (panels c,d) of the SUPER1 ensemble. Only grid points where the anomaly is significant at 95% confidence (*n*=5, see methods) are shown. The green and orange lines indicate, respectively, the pre-eruption average and post-eruption average sea-ice edge.

Figure 7 –Ensemble-mean post-eruption evolution of zonal-mean surface temperature (panel a), zonal-mean 500 hPa zonal wind (panel b) and meridional wind (panel c) anomalies for the SUPER1 ensemble. Positive zonal and meridional winds are, respectively, eastward and northward. Filled contours in panels a,b: Hovmoeller diagrams, only changes statistically significant at 99% confidence are shown. Line plots in panel a: anomalies of equator-to-pole gradient (EPG) for the Northern (top) and Southern (bottom) hemispheres. EPG is defined, for each hemisphere, as the difference between values at the grid latitude closest to the equator and the first grid latitude poleward of 70°. Dotted lines in panels a,c are 98% confidence ranges. A 13-month running-average smoothing has been applied to all data.

Figure 8 - Ensemble-mean simulated anomalies of zonally-integrated atmospheric energy transport at ~60°N (panel a) and ~60°S (c), and oceanic heat transport by advection at 60°N (b) and at 60°S (d) for the SUPER1 ensemble. Lines (shading): mean anomaly (standard error of the mean). Dashed lines indicate the internal variability range (n=5, see methods). Internal variability ranges for the gyre component of ocean heat transport are not shown, since barely distinguishable from that of the total transport. The magenta vertical hatched line indicates the approximate start of the eruptions. Lag(0) corresponds to January of the eruption year. Anomalies are smoothed with a 13-months centered moving average. Positive values correspond to northward transport anomalies (y-axis is

inverted in panels c and d) to ease comparison of poleward transports in the two hemispheres.

Figure 9 – Ensemble-mean simulated annual-average oceanic barotropic streamfunction for integration years 1-2 (panels a, b) and 4-6 (panels c,d) of the SUPER1 ensemble. Only changes statistically significant at 95% confidence are shown. The green and orange lines indicate, respectively, the pre-eruption and post-eruption average winter (top: DJF, bottom: JJA) sea-ice edge.

Figure 10 – Ensemble-mean simulated annual-average mixed layer thickness in two oceanic deep convection regions for integration years 1-2 (panels a, b) and 4-6 (panels c,d) of the SUPER1 ensemble. Only changes statistically significant at 95% confidence are shown. The green and orange lines indicate, respectively, the pre-eruption and post-eruption average winter (top: DJF, bottom: JJA) sea-ice edge.

Figure 11 – Ensemble-mean simulated Southern Hemisphere summer (DJF, top) and winter (JJA, bottom) total net surface energy flux (latent and sensible heat, short- and long-wave radiation, panels a,c) and 10-meter wind anomalies (panels b,d) for integration years 1-2 of the SUPER1 ensemble. Panels a,c: black dots indicate grid points where changes are non significant at the 95% confidence level; panels b,d: only changes statistically significant at 95% confidence for at least one of the wind components are shown

Figure 12 – Ensemble-mean simulated Southern Hemisphere summer (DJF, top) and winter (JJA, bottom) total net surface energy flux (latent and sensible heat, short- and long-wave radiation, panels a,c) and 10-meter wind anomalies (panels b,d) for integration years 4-6 of the SUPER1 ensemble. Panels a,c: black dots indicate grid points where changes are non significant at the 95% confidence level; panels b,d: only changes statistically significant at 95% confidence for at least one of the wind components are shown.

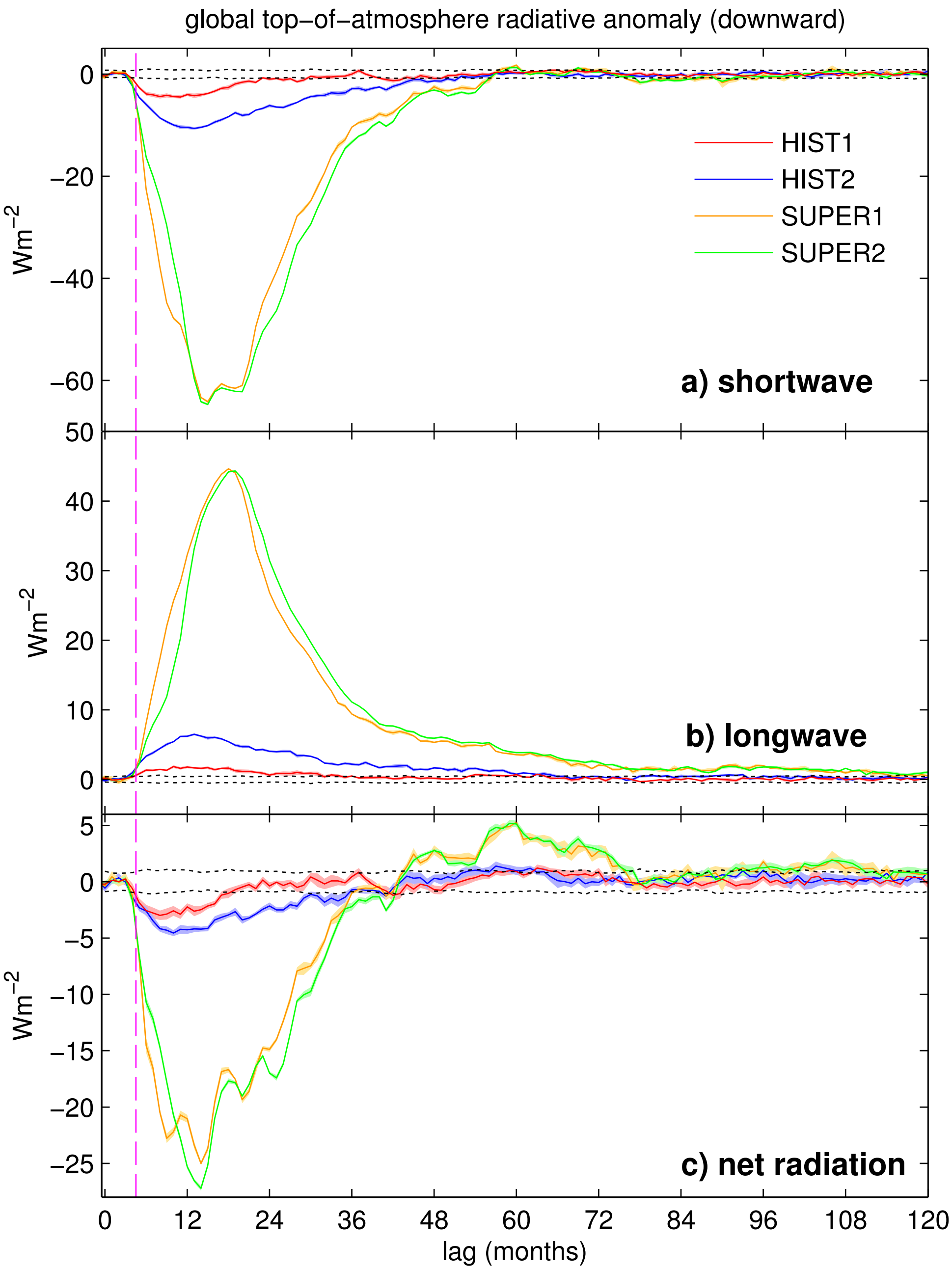

Figure 1 – Simulated imposed forcing in the two historical and the two "supervolcano" ensembles as diagnosed through anomalies in the global-average top-of-atmosphere solar (shortwave, a), thermal (longwave, b) and net (c) radiation. Lines (shading): mean (standard error of the mean). Black dotted lines indicate the internal variability range (n=10, see methods). The magenta vertical hatched line indicates the approximate start of the eruptions. Lag(0) corresponds to January of the eruption year. Positive anomalies correspond to increased downward flux. No smoothing was applied to the series.

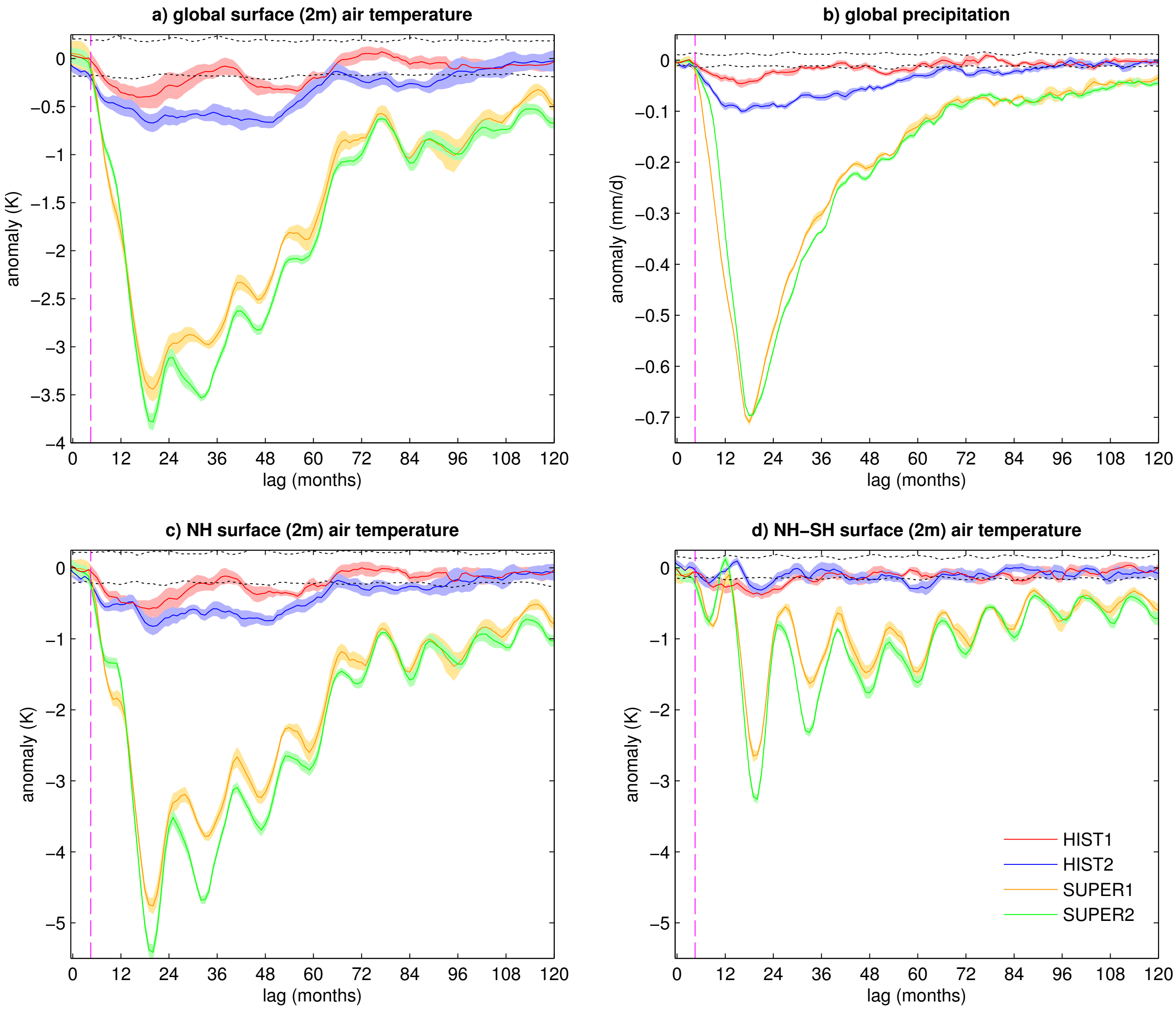

Figure 2 – Simulated post-eruption anomalies of global-average surface (2 meters) air temperature (SAT) (panel a) and total precipitation (b), and Northern-hemispheric average SAT (c) and difference between Northern and Southern-hemispheric average SAT (d) for the two historical and the two "supervolcano" ensembles. Lines (shading): mean (standard error of the mean). Black dashed lines indicate the internal variability range (*n*=10, see methods). The magenta vertical hatched line indicates the approximate start of the eruptions. Lag(0) corresponds to January of the eruption year. Note that the y-axis in panels c and d has the same scale, highlighting the relative magnitude of inter-hemispheric differences in the temperature response.

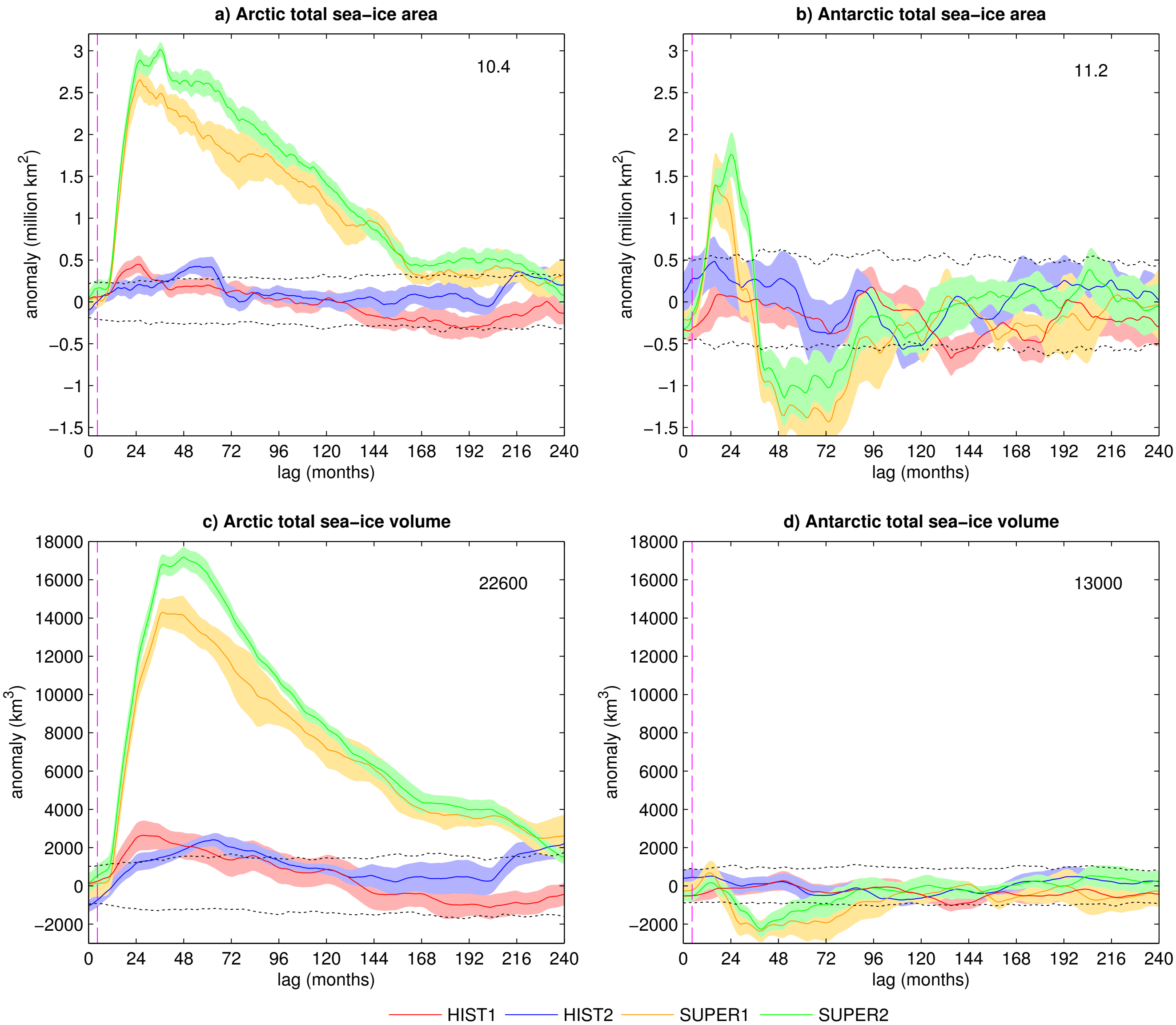

Figure 3 – Simulated post-eruption anomalies of Arctic (top) and Antarctic (bottom) total sea-ice area (top panels) and volume (bottom) for the two historical and the two "supervolcano" ensembles. Lines (shading): mean anomaly (standard error of the mean). Anomalies are smoothed with a 13-months centered moving average. Black dashed lines indicate the internal variability range (n=10¸ see methods). The magenta vertical hatched line indicates the approximate start of the eruptions. Lag(0) corresponds to January of the eruption year. The number on top-right of each panel is the approximate pre-eruption climatology. The y-axis has the same scale in panels a and b, and in panels c and d, highlighting the different magnitude of the hemispheric responses.

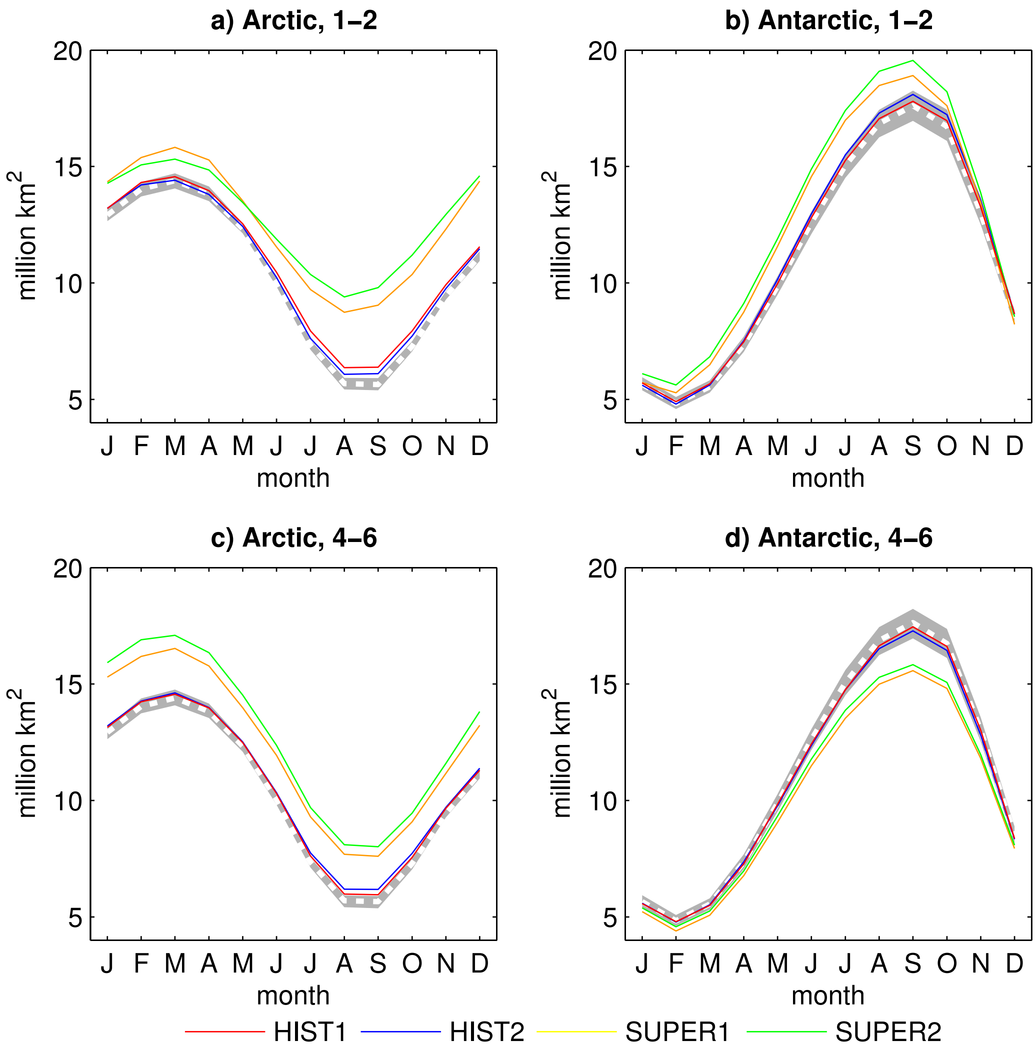

Figure 4 – Ensemble-mean simulated seasonal evolutions of hemispheric sea-ice area for integration years 1-2 (panels a, b) and 4-6 (panels c,d) for the two historical and the two "supervolcano" ensembles. Gray shading (hatched white line) represents the 98% range (mean) for signal occurrence in the control run. Signal in the control run corresponds to the annual evolution averaged over three randomly chosen consecutive years, for a 10-member ensemble.

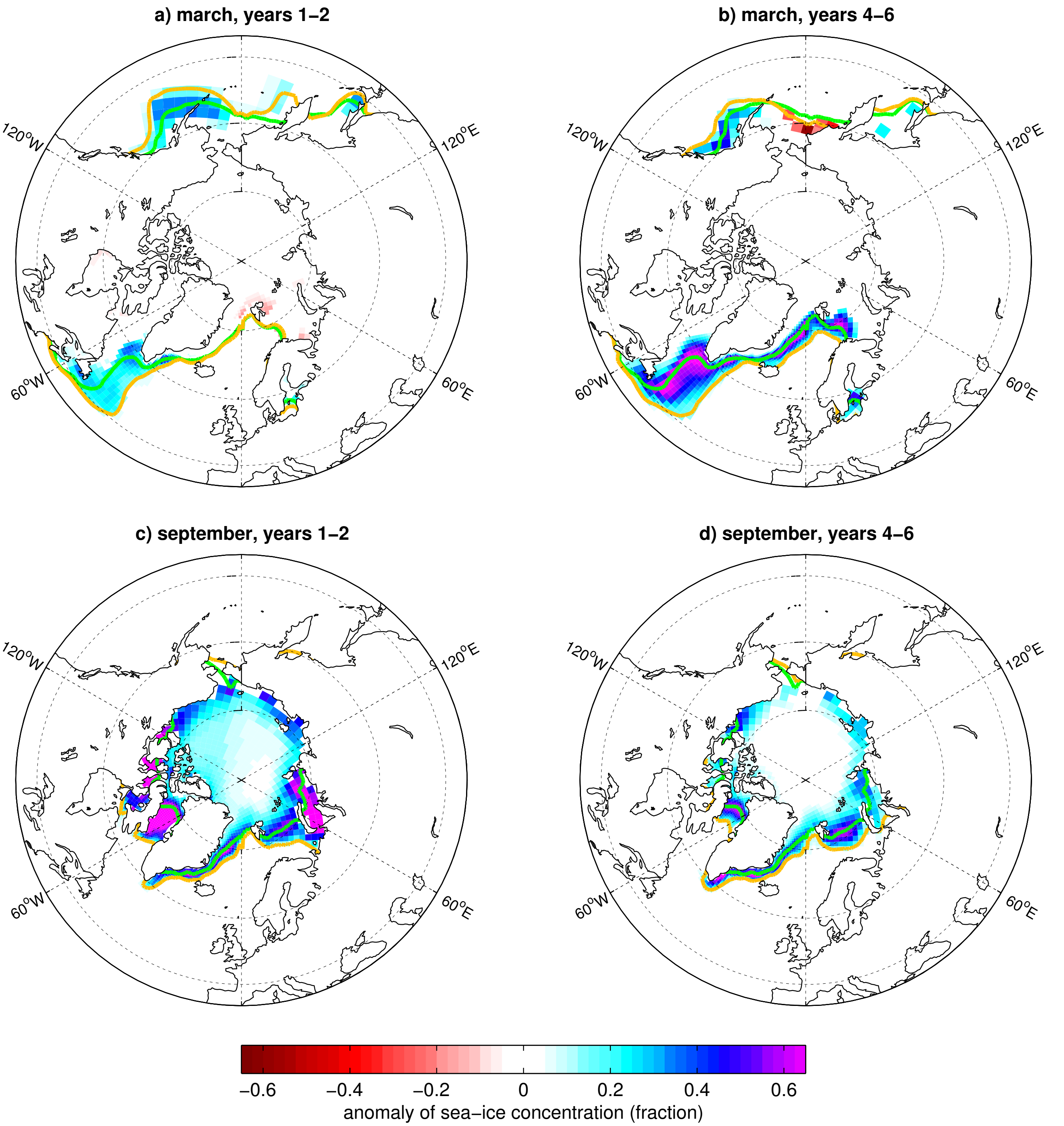

Figure 5 – Ensemble-mean simulated March (top panels) and September (bottom panels) Arctic sea-ice concentration anomalies for integration years 1-2 (panels a, b) and 4-6 (panels c,d) of the SUPER1 ensemble. Only grid points where the anomaly is significant at 95% confidence (*n*=5, see methods) are shown. The green and orange lines indicate, respectively, the pre-eruption average and post-eruption average sea-ice edge.

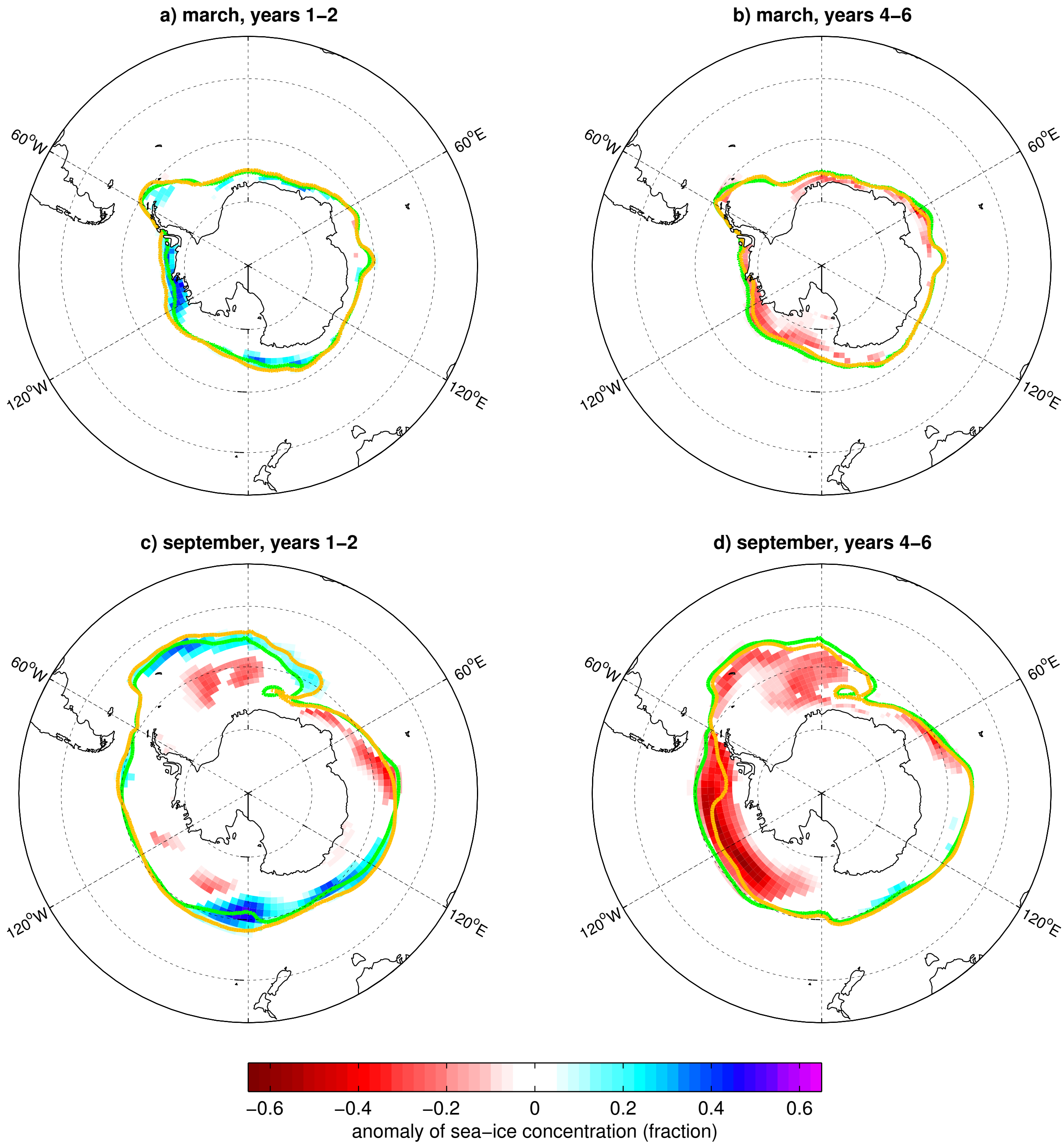

Figure 6 – Ensemble-mean simulated March (top panels) and September (bottom panels) Antarctic sea-ice concentration anomalies for integration years 1-2 (panels a, b) and 4-6 (panels c,d) of the SUPER1 ensemble. Only grid points where the anomaly is significant at 95% confidence (*n*=5, see methods) are shown. The green and orange lines indicate, respectively, the pre-eruption average and post-eruption average sea-ice edge.

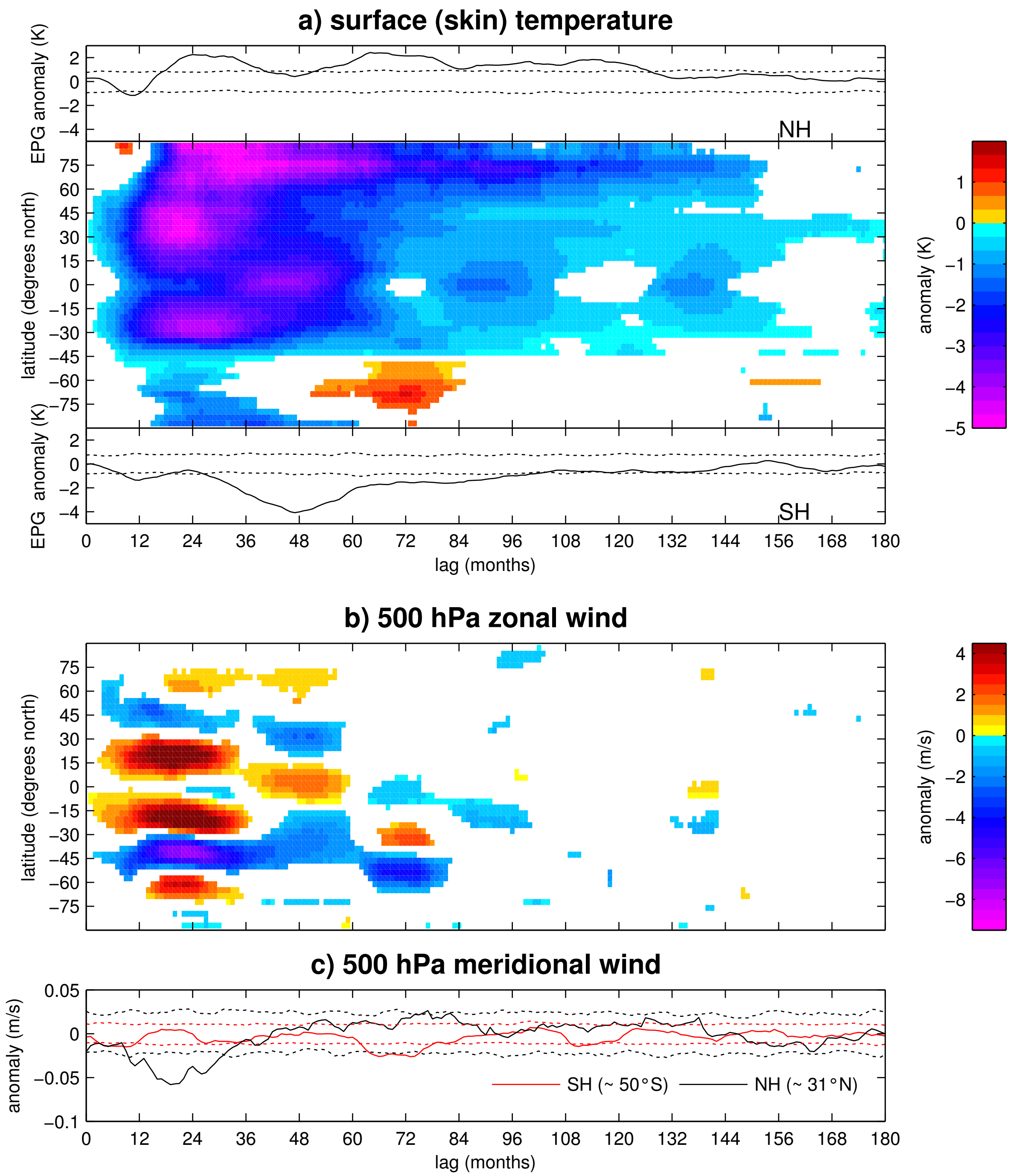

Figure 7 –Ensemble-mean post-eruption evolution of zonal-mean surface temperature (panel a), zonal-mean 500 hPa zonal wind (panel b) and meridional wind (panel c) anomalies for the SUPER1 ensemble. Positive zonal and meridional winds are, respectively, eastward and northward. Filled contours in panels a,b: Hovmoeller diagrams, only changes statistically significant at 99% confidence are shown. Line plots in panel a: anomalies of equator-to-pole gradient (EPG) for the Northern (top) and Southern (bottom) hemispheres. EPG is defined, for each hemisphere, as the difference between values at the grid latitude closest to the equator and the first grid latitude poleward of 70°. Dotted lines in panels a,c are 98% confidence ranges. A 13-month running-average smoothing has been applied to all data.

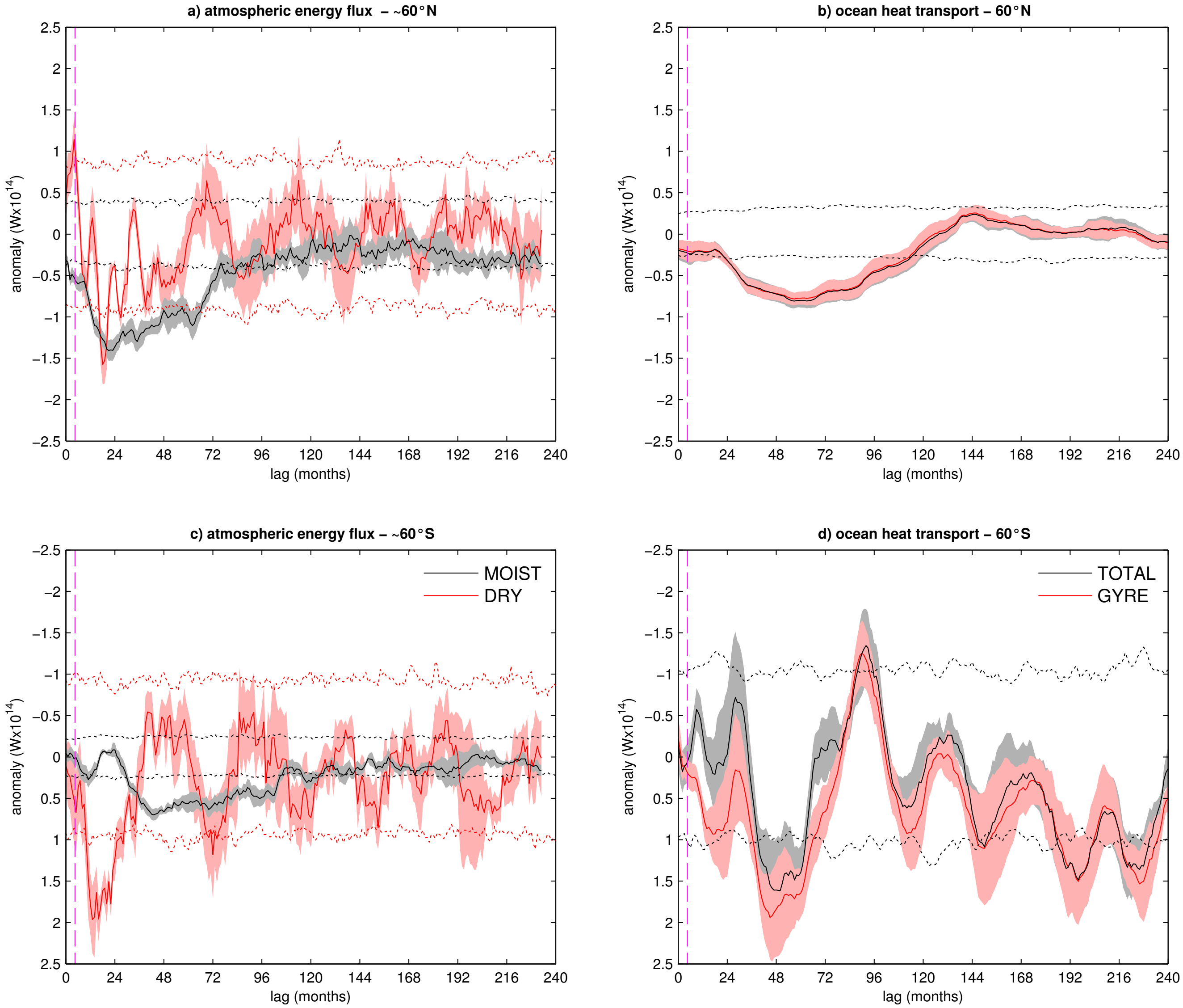

Figure 8 - Ensemble-mean simulated anomalies of zonally-integrated atmospheric energy transport at ~60°N (panel a) and ~60°S (c), and oceanic heat transport by advection at 60°N (b) and at 60°S (d) for the SUPER1 ensemble. Lines (shading): mean anomaly (standard error of the mean). Dashed lines indicate the internal variability range (n=5, see methods). Internal variability ranges for the gyre component of ocean heat transport are not shown, since barely distinguishable from that of the total transport. The magenta vertical hatched line indicates the approximate start of the eruptions. Lag(0) corresponds to January of the eruption year. Anomalies are smoothed with a 13-months centered moving average. Positive values correspond to northward transport anomalies (y-axis is inverted in panels c and d) to ease comparison of poleward transports in the two hemispheres.

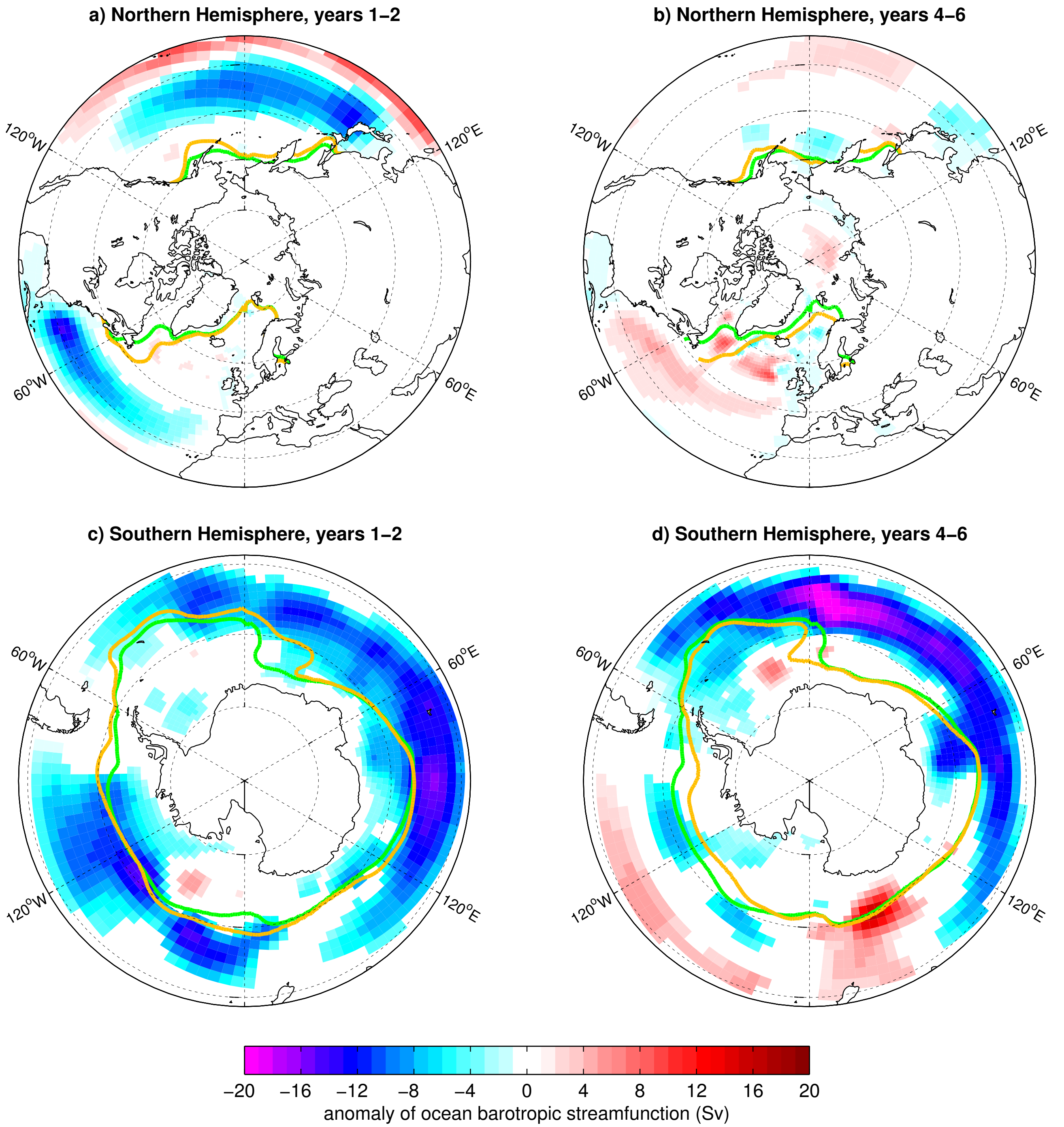

Figure 9 – Ensemble-mean simulated annual-average oceanic barotropic streamfunction for integration years 1-2 (panels a, b) and 4-6 (panels c,d) of the SUPER1 ensemble. Only changes statistically significant at 95% confidence are shown. The green and orange lines indicate, respectively, the pre-eruption and post-eruption average winter (top: DJF, bottom: JJA) sea-ice edge.

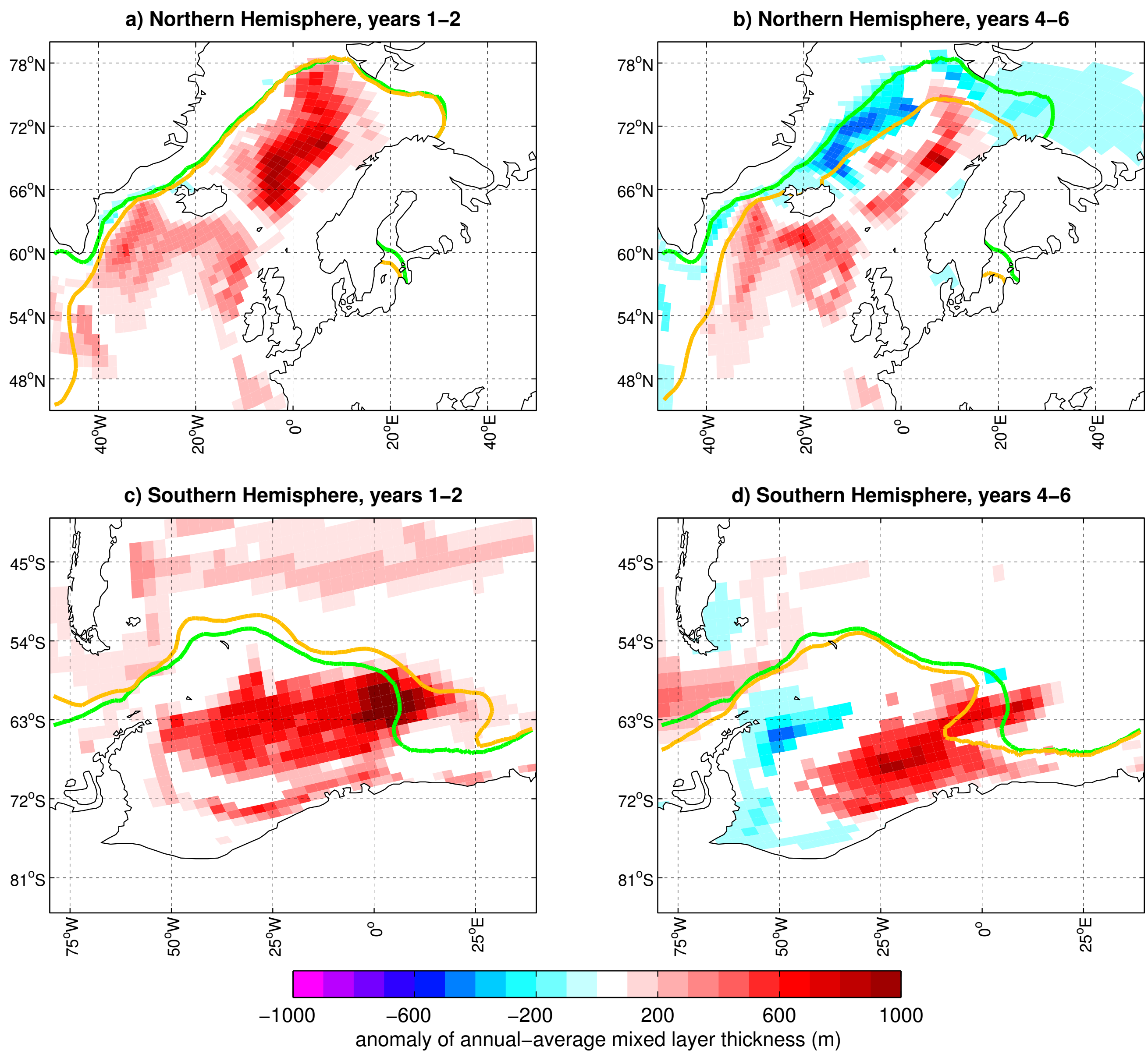

Figure 10 – Ensemble-mean simulated annual-average mixed layer thickness in two oceanic deep convection regions for integration years 1-2 (panels a, b) and 4-6 (panels c,d) of the SUPER1 ensemble. Only changes statistically significant at 95% confidence are shown. The green and orange lines indicate, respectively, the pre-eruption and post-eruption average winter (top: DJF, bottom: JJA) sea-ice edge.

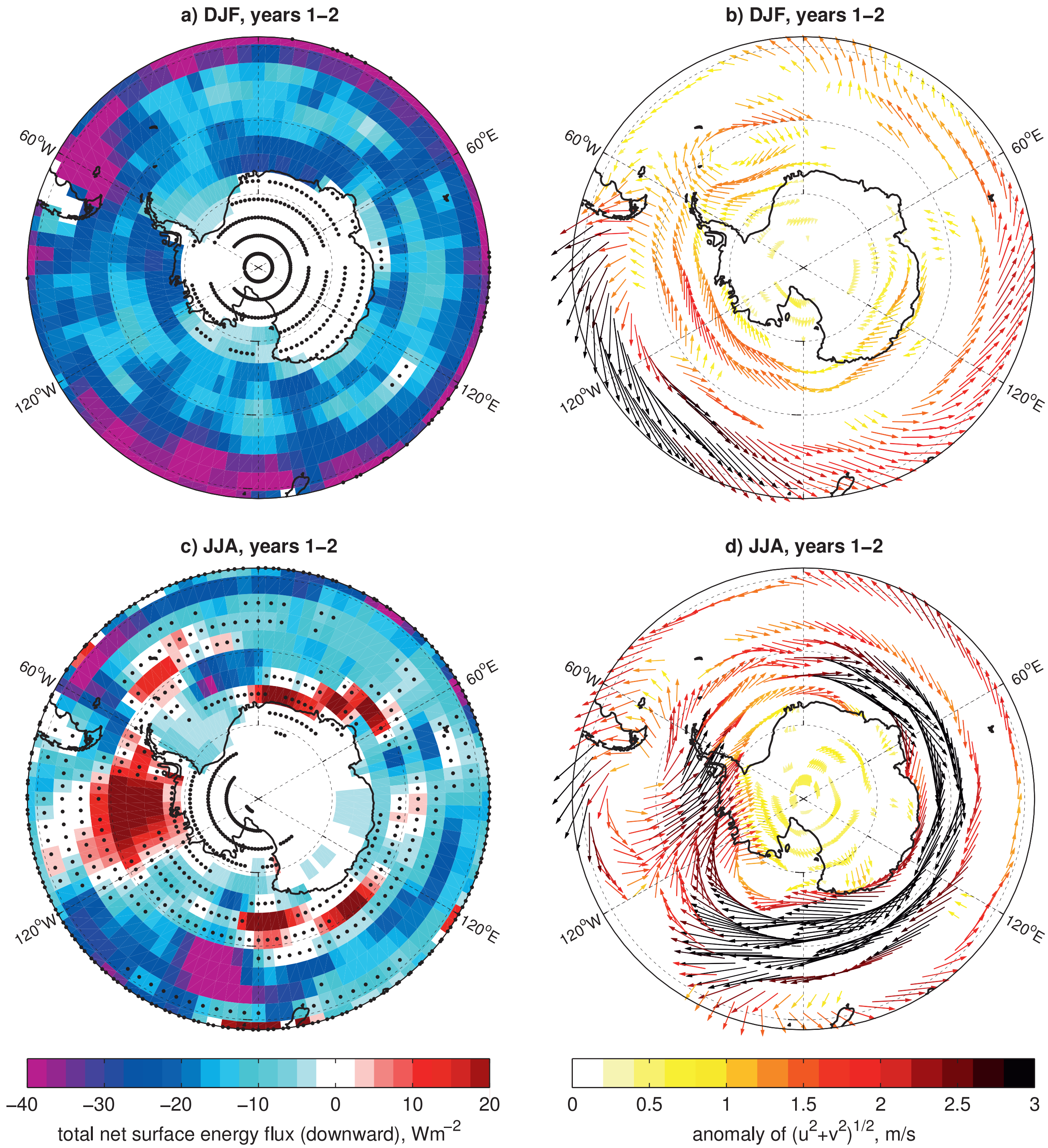

Figure 11 – Ensemble-mean simulated Southern Hemisphere summer (DJF, top) and winter (JJA, bottom) total net surface energy flux (latent and sensible heat, short- and long-wave radiation, panels a,c) and 10-meter wind anomalies (panels b,d) for integration years 1-2 of the SUPER1 ensemble. Panels a,c: black dots indicate grid points where changes are non significant at the 95% confidence level; panels b,d: only changes statistically significant at 95% confidence for at least one of the wind components are shown

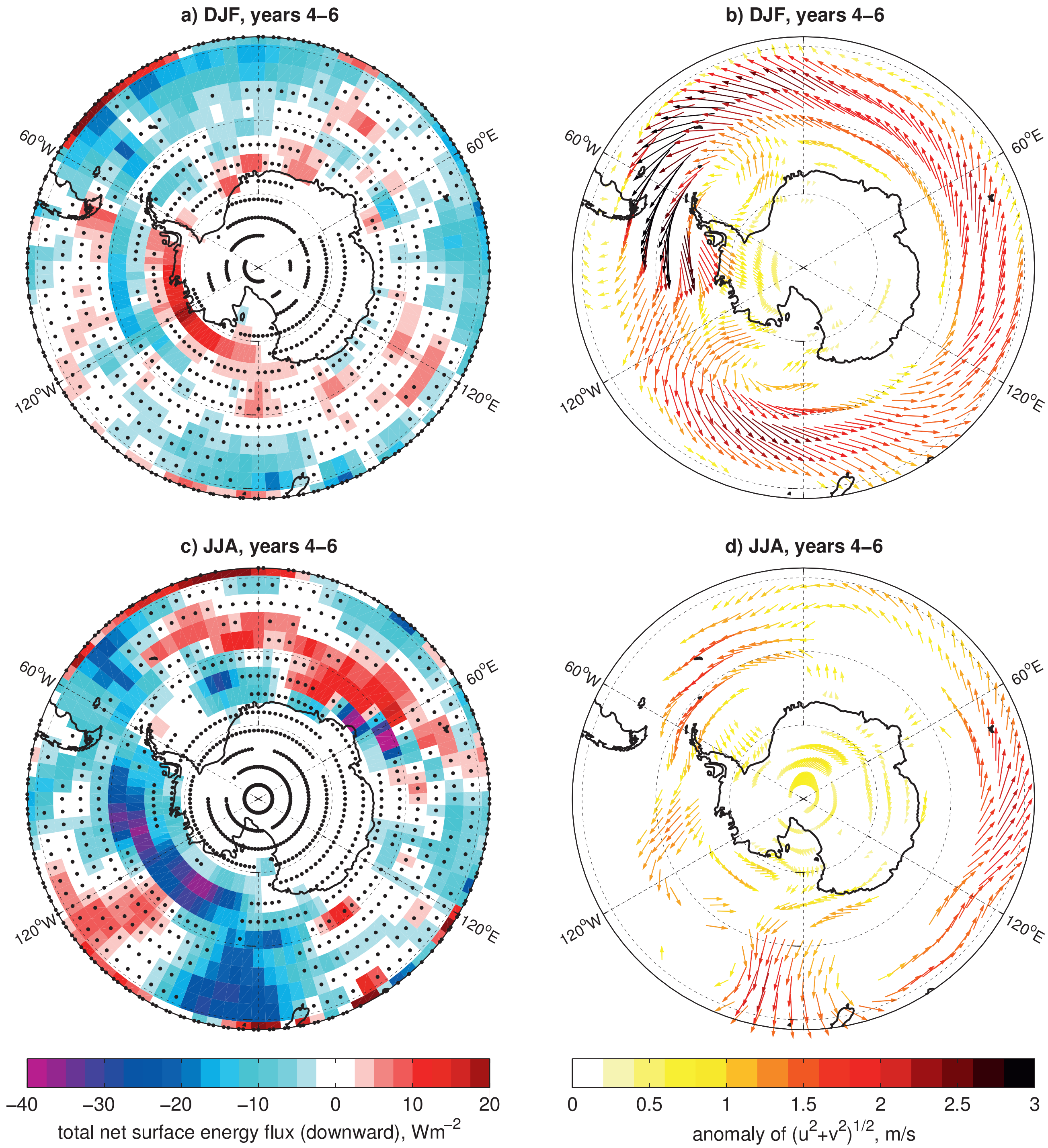

Figure 12 – Ensemble-mean simulated Southern Hemisphere summer (DJF, top) and winter (JJA, bottom) total net surface energy flux (latent and sensible heat, short- and long-wave radiation, panels a,c) and 10-meter wind anomalies (panels b,d) for integration years 4-6 of the SUPER1 ensemble. Panels a,c: black dots indicate grid points where changes are non significant at the 95% confidence level; panels b,d: only changes statistically significant at 95% confidence for at least one of the wind components are shown.